

DESY 95-007
January 1995

Measurement of multiplicity and momentum spectra in the current fragmentation region of the Breit frame at HERA

ZEUS Collaboration

Abstract

Charged particle production has been measured in Deep Inelastic Scattering (DIS) events using the ZEUS detector over a large range of Q^2 from 10 to 1280 GeV^2 . The evolution with Q of the charged multiplicity and scaled momentum has been investigated in the current fragmentation region of the Breit frame. The data are used to study QCD coherence effects in DIS and are compared with corresponding e^+e^- data in order to test the universality of quark fragmentation.

The ZEUS Collaboration

M. Derrick, D. Krakauer, S. Magill, D. Mikunas, B. Musgrave, J. Repond, R. Stanek, R.L. Talaga, H. Zhang
Argonne National Laboratory, Argonne, IL, USA^p

R. Ayad¹, G. Bari, M. Basile, L. Bellagamba, D. Boscherini, A. Bruni, G. Bruni, P. Bruni, G. Cara Romeo, G. Castellini², M. Chiarini, L. Cifarelli³, F. Cindolo, A. Contin, I. Gialas, P. Giusti, G. Iacobucci, G. Laurenti, G. Levi, A. Margotti, T. Massam, R. Nania, C. Nemoz, F. Palmonari, A. Polini, G. Sartorelli, R. Timellini, Y. Zamora Garcia¹, A. Zichichi
University and INFN Bologna, Bologna, Italy^f

A. Bargende, J. Crittenden, K. Desch, B. Diekmann⁴, T. Doeker, M. Eckert, L. Feld, A. Frey, M. Geerts, G. Geitz⁵, M. Grothe, T. Haas, H. Hartmann, D. Haun⁴, K. Heinloth, E. Hilger, H.-P. Jakob, U.F. Katz, S.M. Mari, A. Mass, S. Mengel, J. Mollen, E. Paul, Ch. Rembser, R. Schattevoy⁶, D. Schramm, J. Stamm, R. Wedemeyer
Physikalisches Institut der Universität Bonn, Bonn, Federal Republic of Germany^c

S. Campbell-Robson, A. Cassidy, N. Dyce, B. Foster, S. George, R. Gilmore, G.P. Heath, H.F. Heath, T.J. Llewellyn, C.J.S. Morgado, D.J.P. Norman, J.A. O'Mara, R.J. Tapper, S.S. Wilson, R. Yoshida
H.H. Wills Physics Laboratory, University of Bristol, Bristol, U.K.^o

R.R. Rau
Brookhaven National Laboratory, Upton, L.I., USA^p

M. Arneodo⁷, L. Iannotti, M. Schioppa, G. Susinno
Calabria University, Physics Dept. and INFN, Cosenza, Italy^f

A. Bernstein, A. Caldwell, J.A. Parsons, S. Ritz, F. Sciulli, P.B. Straub, L. Wai, S. Yang, Q. Zhu
Columbia University, Nevis Labs., Irvington on Hudson, N.Y., USA^q

P. Borzemski, J. Chwastowski, A. Eskreys, K. Piotrzkowski, M. Zachara, L. Zawiejski
Inst. of Nuclear Physics, Cracow, Poland^j

L. Adamczyk, B. Bednarek, K. Eskreys, K. Jeleń, D. Kisielewska, T. Kowalski, E. Rulikowska-Zarębska, L. Suszycki, J. Zająć
Faculty of Physics and Nuclear Techniques, Academy of Mining and Metallurgy, Cracow, Poland^j

A. Kotański, M. Przybycień
Jagellonian Univ., Dept. of Physics, Cracow, Poland^k

L.A.T. Bauerdtick, U. Behrens, H. Beier⁸, J.K. Bienlein, C. Coldewey, O. Deppe, K. Desler, G. Drews, M. Flasiński⁹, D.J. Gilkinson, C. Glasman, P. Göttlicher, J. Große-Knetter, B. Gutjahr, W. Hain, D. Hasell, H. Heßling, H. Hultschig, Y. Iga, P. Joos, M. Kasemann, R. Klanner, W. Koch, L. Köpke¹⁰, U. Kötz, H. Kowalski, J. Labs, A. Ladage, B. Löhr, M. Löwe, D. Lüke, O. Mańczak, J.S.T. Ng, S. Nickel, D. Notz, K. Ohrenberg, M. Roco, M. Rohde, J. Roldán, U. Schneekloth, W. Schulz, F. Selonke, E. Stiliaris¹¹, B. Surrow, T. Voß, D. Westphal, G. Wolf, C. Youngman, J.F. Zhou
Deutsches Elektronen-Synchrotron DESY, Hamburg, Federal Republic of Germany

H.J. Grabosch, A. Kharchilava, A. Leich, M. Mattingly, A. Meyer, S. Schlenstedt
DESY-Zeuthen, Inst. für Hochenergiephysik, Zeuthen, Federal Republic of Germany

G. Barbagli, P. Pelfer
University and INFN, Florence, Italy^f

G. Anzivino, G. Maccarrone, S. De Pasquale, L. Votano
INFN, Laboratori Nazionali di Frascati, Frascati, Italy^f

A. Bamberger, S. Eisenhardt, A. Freidhof, S. Söldner-Rembold¹², J. Schroeder¹³, T. Trefzger
Fakultät für Physik der Universität Freiburg i.Br., Freiburg i.Br., Federal Republic of Germany^c

N.H. Brook, P.J. Bussey, A.T. Doyle¹⁴, I. Fleck, V.A. Jamieson, D.H. Saxon, M.L. Utley, A.S. Wilson
Dept. of Physics and Astronomy, University of Glasgow, Glasgow, U.K. ^o

A. Dannemann, U. Holm, D. Horstmann, T. Neumann, R. Sinkus, K. Wick
Hamburg University, I. Institute of Exp. Physics, Hamburg, Federal Republic of Germany ^c

E. Badura¹⁵, B.D. Burow¹⁶, L. Hagge, E. Lohrmann, J. Mainusch, J. Milewski, M. Nakahata¹⁷, N. Pavel, G. Poelz, W. Schott, F. Zetsche
Hamburg University, II. Institute of Exp. Physics, Hamburg, Federal Republic of Germany ^c

T.C. Bacon, I. Butterworth, E. Gallo, V.L. Harris, B.Y.H. Hung, K.R. Long, D.B. Miller, P.P.O. Morawitz, A. Prinias, J.K. Sedgbeer, A.F. Whitfield
Imperial College London, High Energy Nuclear Physics Group, London, U.K. ^o

U. Mallik, E. McCliment, M.Z. Wang, S.M. Wang, J.T. Wu, Y. Zhang
University of Iowa, Physics and Astronomy Dept., Iowa City, USA ^p

P. Cloth, D. Filges
Forschungszentrum Jülich, Institut für Kernphysik, Jülich, Federal Republic of Germany

S.H. An, S.M. Hong, S.W. Nam, S.K. Park, M.H. Suh, S.H. Yon
Korea University, Seoul, Korea ^h

R. Imlay, S. Kartik, H.-J. Kim, R.R. McNeil, W. Metcalf, V.K. Nadendla
Louisiana State University, Dept. of Physics and Astronomy, Baton Rouge, LA, USA ^p

F. Barreiro¹⁸, G. Cases, R. Graciani, J.M. Hernández, L. Hervás¹⁸, L. Labarga¹⁸, J. del Peso, J. Puga, J. Terron, J.F. de Trocóniz
Univer. Autónoma Madrid, Depto de Física Teórica, Madrid, Spain ⁿ

G.R. Smith
University of Manitoba, Dept. of Physics, Winnipeg, Manitoba, Canada ^a

F. Corriveau, D.S. Hanna, J. Hartmann, L.W. Hung, J.N. Lim, C.G. Matthews, P.M. Patel, L.E. Sinclair, D.G. Stairs, M. St.Laurent, R. Ullmann, G. Zacek
McGill University, Dept. of Physics, Montreal, Quebec, Canada ^{a, b}

V. Bashkirov, B.A. Dolgoshein, A. Stifutkin
Moscow Engineering Physics Institute, Moscow, Russia ^l

G.L. Bashindzhyan, P.F. Ermolov, L.K. Gladilin, Y.A. Golubkov, V.D. Kobrin, V.A. Kuzmin, A.S. Proskuryakov, A.A. Savin, L.M. Shcheglova, A.N. Solomin, N.P. Zotov
Moscow State University, Institute of Nuclear Physics, Moscow, Russia ^m

M. Botje, F. Chlebana, A. Dake, J. Engelen, M. de Kamps, P. Kooijman, A. Kruse, H. Tiecke, W. Verkerke, M. Vreeswijk, L. Wiggers, E. de Wolf, R. van Woudenberg
NIKHEF and University of Amsterdam, Netherlands ⁱ

D. Acosta, B. Bylsma, L.S. Durkin, K. Honscheid, C. Li, T.Y. Ling, K.W. McLean¹⁹, W.N. Murray, I.H. Park, T.A. Romanowski²⁰, R. Seidlein²¹
Ohio State University, Physics Department, Columbus, Ohio, USA ^p

D.S. Bailey, G.A. Blair²², A. Byrne, R.J. Cashmore, A.M. Cooper-Sarkar, D. Daniels²³, R.C.E. Devenish, N. Harnew, M. Lancaster, P.E. Luffman²⁴, L. Lindemann, J.D. McFall, C. Nath, A. Quadt, H. Uijterwaal, R. Walczak, F.F. Wilson, T. Yip
Department of Physics, University of Oxford, Oxford, U.K. ^o

G. Abbiendi, A. Bertolin, R. Brugnera, R. Carlin, F. Dal Corso, M. De Giorgi, U. Dosselli, S. Limentani, M. Morandin, M. Posocco, L. Stanco, R. Stroili, C. Voci
Dipartimento di Fisica dell' Università and INFN, Padova, Italy ^f

J. Bulmahn, J.M. Butterworth, R.G. Feild, B.Y. Oh, J.J. Whitmore²⁵
Pennsylvania State University, Dept. of Physics, University Park, PA, USA ^q

G. D'Agostini, G. Marini, A. Nigro, E. Tassi
Dipartimento di Fisica, Univ. 'La Sapienza' and INFN, Rome, Italy ^f

J.C. Hart, N.A. McCubbin, K. Prytz, T.P. Shah, T.L. Short
Rutherford Appleton Laboratory, Chilton, Didcot, Oxon, U.K. ^o

E. Barberis, N. Cartiglia, T. Dubbs, C. Heusch, M. Van Hook, B. Hubbard, W. Lockman,
J.T. Rahn, H.F.-W. Sadrozinski, A. Seiden
University of California, Santa Cruz, CA, USA ^p

J. Biltzinger, R.J. Seifert, A.H. Walenta, G. Zech
Fachbereich Physik der Universität-Gesamthochschule Siegen, Federal Republic of Germany ^c

H. Abramowicz, G. Briskin, S. Dagan²⁶, A. Levy²⁷
School of Physics, Tel-Aviv University, Tel Aviv, Israel ^e

T. Hasegawa, M. Hazumi, T. Ishii, M. Kuze, S. Mine, Y. Nagasawa, M. Nakao, I. Suzuki, K. Tokushuku, S. Yamada, Y. Yamazaki
Institute for Nuclear Study, University of Tokyo, Tokyo, Japan ^g

M. Chiba, R. Hamatsu, T. Hirose, K. Homma, S. Kitamura, Y. Nakamitsu, K. Yamauchi
Tokyo Metropolitan University, Dept. of Physics, Tokyo, Japan ^g

R. Cirio, M. Costa, M.I. Ferrero, L. Lamberti, S. Maselli, C. Peroni, R. Sacchi, A. Solano, A. Staiano
Universita di Torino, Dipartimento di Fisica Sperimentale and INFN, Torino, Italy ^f

M. Dardo
II Faculty of Sciences, Torino University and INFN - Alessandria, Italy ^f

D.C. Bailey, D. Bandyopadhyay, F. Benard, M. Brkic, M.B. Crombie, D.M. Gingrich²⁸, G.F. Hartner, K.K. Joo, G.M. Levman, J.F. Martin, R.S. Orr, C.R. Sampson, R.J. Teuscher
University of Toronto, Dept. of Physics, Toronto, Ont., Canada ^a

C.D. Catterall, T.W. Jones, P.B. Kaziewicz, J.B. Lane, R.L. Saunders, J. Shulman
University College London, Physics and Astronomy Dept., London, U.K. ^o

K. Blankenship, J. Kochocki, B. Lu, L.W. Mo
Virginia Polytechnic Inst. and State University, Physics Dept., Blacksburg, VA, USA ^q

W. Bogusz, K. Charchuła, J. Ciborowski, J. Gajewski, G. Grzelak, M. Kasprzak, M. Krzyżanowski, K. Muchorowski, R.J. Nowak, J.M. Pawlak, T. Tymieniecka, A.K. Wróblewski, J.A. Zakrzewski, A.F. Żarnecki
Warsaw University, Institute of Experimental Physics, Warsaw, Poland ^j

M. Adamus
Institute for Nuclear Studies, Warsaw, Poland ^j

Y. Eisenberg²⁶, U. Karshon²⁶, D. Revel²⁶, D. Zer-Zion
Weizmann Institute, Nuclear Physics Dept., Rehovot, Israel ^d

I. Ali, W.F. Badgett, B. Behrens, S. Dasu, C. Fordham, C. Foudas, A. Goussiou, R.J. Loveless, D.D. Reeder, S. Silverstein, W.H. Smith, A. Vaiciulis, M. Wodarczyk
University of Wisconsin, Dept. of Physics, Madison, WI, USA ^p

T. Tsurugai
Meiji Gakuin University, Faculty of General Education, Yokohama, Japan

S. Bhadra, M.L. Cardy, C.-P. Fagerstroem, W.R. Frisken, K.M. Furutani, M. Khakzad, W.B. Schmidke
York University, Dept. of Physics, North York, Ont., Canada ^a

¹ supported by Worldlab, Lausanne, Switzerland
² also at IROE Florence, Italy
³ now at Univ. of Salerno and INFN Napoli, Italy
⁴ now a self-employed consultant
⁵ on leave of absence
⁶ now at MPI Berlin
⁷ now also at University of Torino
⁸ presently at Columbia Univ., supported by DAAD/HSPII-AUFE
⁹ now at Inst. of Computer Science, Jagellonian Univ., Cracow
¹⁰ now at Univ. of Mainz
¹¹ supported by the European Community
¹² now with OPAL Collaboration, Faculty of Physics at Univ. of Freiburg
¹³ now at SAS-Institut GmbH, Heidelberg
¹⁴ also supported by DESY
¹⁵ now at GSI Darmstadt
¹⁶ also supported by NSERC
¹⁷ now at Institute for Cosmic Ray Research, University of Tokyo
¹⁸ on leave of absence at DESY, supported by DGICYT
¹⁹ now at Carleton University, Ottawa, Canada
²⁰ now at Department of Energy, Washington
²¹ now at HEP Div., Argonne National Lab., Argonne, IL, USA
²² now at RHBNC, Univ. of London, England
²³ Fulbright Scholar 1993-1994
²⁴ now at Cambridge Consultants, Cambridge, U.K.
²⁵ on leave and partially supported by DESY 1993-95
²⁶ supported by a MINERVA Fellowship
²⁷ partially supported by DESY
²⁸ now at Centre for Subatomic Research, Univ. of Alberta, Canada and TRIUMF, Vancouver, Canada

a supported by the Natural Sciences and Engineering Research Council of Canada (NSERC)
b supported by the FCAR of Quebec, Canada
c supported by the German Federal Ministry for Research and Technology (BMFT)
d supported by the MINERVA Gesellschaft für Forschung GmbH, and by the Israel Academy of Science
e supported by the German Israeli Foundation, and by the Israel Academy of Science
f supported by the Italian National Institute for Nuclear Physics (INFN)
g supported by the Japanese Ministry of Education, Science and Culture (the Monbusho) and its grants for Scientific Research
h supported by the Korean Ministry of Education and Korea Science and Engineering Foundation
i supported by the Netherlands Foundation for Research on Matter (FOM)
j supported by the Polish State Committee for Scientific Research (grant No. SPB/P3/202/93) and the Foundation for Polish-German Collaboration (proj. No. 506/92)
k supported by the Polish State Committee for Scientific Research (grant No. PB 861/2/91 and No. 2 2372 9102, grant No. PB 2 2376 9102 and No. PB 2 0092 9101)
l partially supported by the German Federal Ministry for Research and Technology (BMFT)
m supported by the German Federal Ministry for Research and Technology (BMFT), the Volkswagen Foundation, and the Deutsche Forschungsgemeinschaft
n supported by the Spanish Ministry of Education and Science through funds provided by CICYT
o supported by the Particle Physics and Astronomy Research Council
p supported by the US Department of Energy
q supported by the US National Science Foundation

1 Introduction

A widely studied topic of perturbative Quantum Chromodynamics (pQCD) is the nature of the quark fragmentation process from the quark-antiquark pair created in e^+e^- annihilation experiments. The purpose of this paper is to compare the fragmentation properties of the struck quark in Deep Inelastic Scattering (DIS) to those of the quarks produced in such e^+e^- annihilation experiments, in order to test the universality of the quark fragmentation process.

Operation of the HERA electron-proton collider has vastly extended the kinematic range for studies of the hadronic final state in DIS. The event kinematics of DIS are determined by the negative square of the four-momentum transfer, $Q^2 \equiv -q^2$, and the Bjorken scaling variable, $x = Q^2/2P \cdot q$, where P is the four-momentum of the proton. In the Quark Parton Model (QPM), the interacting quark from the proton carries the four-momentum xP . The variable y , the fractional energy transfer to the proton in its rest frame, is related to x and Q^2 by $y = Q^2/xs$, where \sqrt{s} is the electron-proton centre of mass energy.

A natural frame to study the dynamics of the hadronic final state in DIS is the Breit frame [1]. In this frame the exchanged virtual boson is completely space-like and is given by $q = (0, 0, 0, -Q = -2xP^B) \equiv (E, p_x, p_y, p_z)$ where P^B is the proton momentum in the Breit frame. In the QPM the z -component of the momentum of the incoming quark is $Q/2$ before and $-Q/2$ after the interaction with the exchanged virtual boson. The particles produced in the DIS interaction can then be assigned to one of two regions. The current region corresponds to the direction of the outgoing struck quark in the QPM. In this paper we define the current region corresponding to particles with $p_z < 0$, whilst the target region is defined by $p_z > 0$.

In e^+e^- annihilation the two quarks are produced with equal and opposite momenta, $\pm\sqrt{s}/2$. In the Breit frame of DIS, a quark is struck from within the proton with outgoing momentum $-Q/2$. In the direction of the struck quark the particle spectra are expected to have no dependence on x and a dependence on Q similar to those observed in e^+e^- annihilation [2, 3, 4] at energy $\sqrt{s} = Q$.

The results from e^+e^- annihilation support the inclusion of coherence effects in pQCD [5, 6, 7, 8]. The phenomenon of coherence is a natural consequence of the quantum mechanical treatment of the parton cascade. As long wavelength gluons are unable to resolve individual colour charges of partons within the parton cascade, the available phase space for soft gluon emissions is reduced to an angular-ordered region, due to destructive interference. This leads to a number of important differences in the properties of the partonic final state relative to the incoherent case. The most notable of these are the slower rise in the multiplicity of partons with increasing energy and the modification of the logarithmic parton momentum spectra to an approximately Gaussian form, which is often referred to as the “hump-backed” plateau [8].

Coherence effects are explicitly included in the Modified Leading Log Approximation (MLLA) [2] of pQCD. The MLLA calculations predict the parton multiplicity and the form of the momentum spectra from quark fragmentation at a given, sufficiently large, energy. The hypothesis of Local Parton Hadron Duality (LPHD) [9], which relates the observed hadron distributions to the calculated parton distributions via a constant of proportionality κ^{ch} , is used in conjunction with the predictions of the MLLA. Using this assumption the modifications due to coherence are therefore not only expected to be experimentally observed, but the MLLA calculations should also be directly applicable to data.

So far these effects have been studied at e^+e^- annihilation experiments [10, 11, 12] using the average charged particle multiplicity, $\langle n_{ch} \rangle$, and the distribution of the scaled momentum, $\ln(1/x_p)$, where $x_p = 2p/\sqrt{s}$. The results from these experiments are in accordance with the MLLA and the assumptions of LPHD.

Previous fixed-target DIS ($\bar{\nu}p$) measurements in the Breit frame have been performed in the range $1 < Q^2 < 45 \text{ GeV}^2$ with a mean $\bar{\nu}$ beam energy of 33 GeV [13]. In the present paper the scaled momentum and charged multiplicity distributions of the hadronic final state are measured in the current region of the Breit frame as a function of x and Q in the range $6 \times 10^{-4} < x < 5 \times 10^{-2}$ and $10 < Q^2 < 1280 \text{ GeV}^2$ with a mean energy of the electron beam measured in the proton rest frame $\sim 10^4 \text{ GeV}$. Comparisons are made with Monte Carlo models, MLLA analytic calculations and e^+e^- data. The DIS data were obtained in 1993 with the ZEUS detector at the HERA collider where electrons of energy $E_e = 26.7 \text{ GeV}$ collided with protons of energy $E_p = 820 \text{ GeV}$, and correspond to an integrated luminosity of 0.55 pb^{-1} .

2 The ZEUS detector and trigger

ZEUS is a multipurpose magnetic detector which has been described elsewhere [14, 15]. Here we give a brief description concentrating on those parts of the detector relevant for the present analysis.

Charged particles are tracked by the inner tracking detectors which operate in a magnetic field of 1.43 T provided by a thin superconducting coil. Immediately surrounding the beampipe is the vertex detector (VXD) which consists of 120 radial cells, each with 12 sense wires [16]. The achieved resolution is $50 \mu\text{m}$ in the central region of a cell and $150 \mu\text{m}$ near the edges. Surrounding the VXD is the central tracking detector (CTD) which consists of 72 cylindrical drift chamber layers, organised into 9 ‘superlayers’ [17]. These superlayers alternate between those with wires parallel (axial) to the collision axis and those inclined at a small angle to give a stereo view. The magnetic field is significantly inhomogeneous towards the ends of the CTD thus complicating the electron drift. With the present understanding of the chamber, a spatial resolution of $260 \mu\text{m}$ has been achieved. The hit efficiency of the chamber is greater than 95%.

In events with charged particle tracks, using the combined data from both chambers, reconstructed primary vertex position resolutions of 0.6 cm in the Z direction and 0.1 cm in the XY plane are measured. (The ZEUS coordinate system is defined as right handed with the Z axis pointing in the proton beam direction and the X axis horizontal pointing towards the centre of HERA. The polar angle θ is defined with respect to the Z -direction.) The resolution in transverse momentum for full length tracks is $\sigma_{p_T}/p_T = 0.005p_T \oplus 0.016$ (for p_T in GeV).

The solenoid is surrounded by a high resolution uranium-scintillator calorimeter divided into three parts, forward (FCAL), barrel (BCAL) and rear (RCAL). Holes of $20 \times 20 \text{ cm}^2$ in the centre of FCAL and RCAL are required to accommodate the HERA beam pipe. Each of the calorimeter parts is subdivided into towers which in turn are segmented longitudinally into electromagnetic (EMC) and hadronic (HAC) sections. These sections are further subdivided into cells, which are read out by two photomultiplier tubes. A detailed description of the calorimeter is given in [18].

For measuring the luminosity as well as for tagging very small Q^2 processes, two lead-scintillator calorimeters are used [19]. Bremsstrahlung photons emerging from the electron-proton interaction point (IP) at angles $\theta_\gamma \leq 0.5$ mrad with respect to the electron beam axis hit the photon calorimeter at 107 m from the IP. Electrons emitted from the IP at scattering angles less than 6 mrad and with energies, E'_e , between $0.2E_e$ and $0.9E_e$ are deflected by beam magnets and hit the electron calorimeter placed 35 m from the IP.

For events with the scattered electron detected in the calorimeter, the trigger was essentially independent of the DIS hadronic final state. The trigger acceptance was greater than 97% for $Q^2 > 10$ GeV 2 and independent of Q^2 [20].

3 Event selection

The offline selection of DIS events was similar to that described in our earlier publications [21-26]. Scattered electron candidates were selected by using the pattern of energy deposition in the calorimeter. The electron identification algorithm was tuned for purity rather than efficiency. In studies with Monte Carlo DIS events and test beam data the purity was estimated to be $\geq 96\%$ for $E'_e \geq 10$ GeV.

The ZEUS detector is almost hermetic, allowing the kinematic variables x and Q^2 to be reconstructed in a variety of ways using combinations of electron and hadronic system energies and angles. Measurements made purely from the measurement of the scattered electron energy and angle, are denoted with a subscript e whilst those made purely from the hadronic system, by the Jacquet-Blondel method, are denoted by the subscript JB [27]. The double angle method which calculates the kinematic variables from the scattered electron angle and the angle of the struck quark, γ_H , as calculated from the final hadronic system are denoted by the subscript DA [28].

In the kinematic region selected, the optimal method of determining Q^2 , x and the boost, $\vec{\beta}$, from the laboratory to the Breit frame is based on the DA method.

For our final event selection we demanded

- $E'_e \geq 10$ GeV, to achieve a high purity sample of DIS events;
- $Q_{DA}^2 \geq 10$ GeV 2 ;
- $y_e \leq 0.95$, to reduce the photoproduction background;
- $y_{JB} \geq 0.04$, to give sufficient accuracy for DA reconstruction;
- $\delta = \sum_i E_i(1 - \cos \theta_i) \geq 35$ GeV, where the sum runs over all calorimeter cells. The measured energy of the cell is denoted by E_i and its polar angle with respect to the incident proton beam by θ_i . Nominally, δ should peak at twice the electron beam energy, 53.4 GeV. This cut is used to remove photoproduction events and to control radiative corrections.

Furthermore we required

- a primary vertex position, determined from VXD and CTD tracks, in the range $-50 \leq Z_{vtx} \leq 40$ cm and a cut on the radial distance from the beamline $R_{vtx} = \sqrt{X_{vtx}^2 + Y_{vtx}^2} < 10$ cm;
- the impact point (X, Y) of the scattered electron in the RCAL to lie outside a square of 32×32 cm 2 centred on the beam axis, to ensure the electron is fully contained within the detector and its position can be reconstructed with sufficient accuracy;
- no more than 5 GeV of energy deposition in the electron calorimeter of the luminosity detector, to exclude potential photoproduction background events.

Following these cuts, the remaining photoproduction background was estimated to be $\simeq 1\%$ using events tagged in the luminosity detector. The contamination from beam-gas background was estimated to be below 0.5% from unpaired electron and proton bunches. Finally, we rejected QED Compton scattering events and residual cosmic and beam-related muons.

A total of 31.5K events was selected in this way corresponding to an integrated luminosity of 0.55 pb $^{-1}$. Of these events about 8-10% [23] contain a large rapidity gap in the hadronic final state. These are characterised by $\eta_{max} < 1.5$, where η_{max} is the maximum pseudorapidity of any calorimeter cluster in the event. Here, the pseudorapidity is defined by $\eta = -\ln(\tan(\theta/2))$ and a cluster is an isolated set of adjacent cells with summed energy above 400 MeV.

4 Track reconstruction and selection

Two programs for track finding and fitting have been developed independently which follow different strategies in the pattern recognition and track fitting stages.

In the first approach, adopted for the final data analysis, the track finding algorithm starts with hits in the outermost axial superlayers of the CTD. As the trajectory is followed inwards to the beam axis, more hits from the axial wires and the VXD are incorporated. The resulting circle in the XY projection is used for the pattern recognition in the stereo superlayer pattern. The momentum vector is determined in a 5-parameter helix fit.

The other track finding program is based on the Kalman filtering technique [29]. Seed tracks found in the outer layers of the CTD are extended inwards and points are added as wire layers of the CTD are crossed. The track parameters at each step are updated using the Kalman method. In the second step a Kalman fit to the points found in the pattern recognition phase is performed taking into account non-linear corrections to the measured drift time. Following the reconstructed CTD track inwards, CTD and VXD hits are associated to the track. The CTD tracks are merged to VXD track segments using the Kalman filtering algorithm.

Multiple Coulomb scattering in the beampipe, and the walls of the VXD and CTD were taken into account in the evaluation of the covariance matrix. The vertex fit is performed with the fitted tracks using the perigee parameterisation [30]. The vertex position is evaluated and the track parameters at the vertex are re-evaluated.

The reconstructed tracks used in this analysis are associated with the primary event vertex and have $p_T > 200$ MeV and $|\eta| < 1.5$, corresponding to the polar angle region between 25° and 155° . This is a region of good CTD acceptance where the detector response and systematics are best understood. For tracks within the fiducial volume defined by these cuts, the track reconstruction efficiency is $\simeq 95\%$.

The Breit frame boost was reconstructed using the scattered electron, where the energy was determined using the *DA* formula and the polar and azimuthal angles were measured from the impact point on the calorimeter. The four-momentum vectors of the charged particles were boosted to the Breit frame, assuming the pion mass to determine the particle's energy, and were assigned to the current region if $p_z < 0$ in the Breit frame.

Monte Carlo simulations were used to determine the acceptance for tracks in the current region as a function of (x, Q^2) . The chosen analysis intervals in (x, Q^2) correspond to regions of high acceptance $\gtrsim 70\%$ in the current region of the Breit frame. These intervals are commensurate with the resolution of x and Q^2 .

The measured variables in the analysis are the inclusive mean charged multiplicity, $\langle n_{ch} \rangle$, in the current region of the Breit frame and the distributions of $\ln(1/x_p)$. Here, $x_p = 2p/Q$, which is the momentum p of a track from the primary vertex measured in the Breit frame, scaled by $Q/2$, the maximum possible momentum (ignoring effects due to intrinsic k_T of the quark within the proton). The peak position of the $\ln(1/x_p)$ distribution is denoted by $\ln(1/x_p)_{max}$.

Uncertainty in the reconstruction of the boost vector, $\vec{\beta}$, was found to be the most significant factor on the resolution of $\ln(1/x_p)$. Near the peak position of the $\ln(1/x_p)$ distributions the resolution is $\simeq 0.15$ units, with no significant shift around the peak position, leading to a choice of bin width of 0.25 units. Migration of tracks from the current region to the target region was typically $\simeq 8\%$. The migration into the current region from the target fragmentation region is of a similar magnitude as the migration out. At low values of y , however, the level of migration is up to $\simeq 25\%$. In the low y region, the hadronic activity is low and the measurement of γ_H becomes distorted by noise in the calorimeter leading to a reduced x resolution and hence an uncertainty in $\vec{\beta}$.

5 QCD models and event simulation

Monte Carlo event simulation is used to correct for acceptance and resolution effects. The detector simulation is based on the GEANT 3.13 [31] program and incorporates our best knowledge of the apparatus. Details of the detector (MOZART) and trigger (ZGANA) simulation codes are given in [14].

Neutral current DIS events with $Q^2 > 4$ GeV 2 were generated using the HERACLES 4.4 program [32] which incorporates first order electroweak corrections. The Monte Carlo generator LEPTO 6.1 [33], interfaced to HERACLES via the program DJANGO 6.0 [34], was used to simulate QCD cascades and fragmentation. The parton cascade was modelled in different ways:

- with the colour-dipole model including the boson-gluon fusion process (CDMBGF), using the ARIADNE 4.03 [35] program. In this model coherence effects are implicitly included in the formalism of the parton cascade; and,

- using the matrix element plus parton showers option (MEPS) within LEPTO, where coherence effects in the final state cascade are included by angular ordering of successive parton emissions.

These models use the Lund string fragmentation model [36] for the hadronisation phase as implemented in JETSET 7.3 [37]. An additional sample of events was generated with the HERWIG 5.7 Monte Carlo [38], where no electroweak radiative corrections were applied. The parton cascade includes coherence effects in a manner similar to that of LEPTO and a clustering model is used for the hadronisation [7, 39].

For ARIADNE and HERWIG the parameterisation of the parton distribution functions was the MRSD' set [40]. The GRV [41] parameterisation was used for the MEPS data set. These parameterisations have been shown to describe reasonably the HERA measurements of the proton structure function, F_2 [21, 42].

Whilst these programs give a reasonable description of the observed energy flow [22] they do not describe the excess of events observed with a large rapidity gap. The properties of these diffractive events are consistent with the exchange of a pomeron between the proton and virtual photon. The POMPYT Monte Carlo [43] models high-energy diffractive processes where the proton emits such a pomeron whose constituents take part in a hard scattering process with the virtual photon. A hard quark density distribution for the pomeron provides an acceptable description of this class of events [26]. The Monte Carlo program based on the model of Nikolaev-Zakharov [44] also gives an acceptable description of this class of events.

For each of the above Monte Carlo programs the default parameters were used. The Monte Carlo event samples were passed through reconstruction and selection procedures identical to those for the data.

6 Data correction

The correction procedure is based on the detailed Monte Carlo simulation of the ZEUS detector with the event generators described in the previous section. Since the ARIADNE model gives the best overall description of our observed energy flow [22] it is used for the standard corrections and unfolding of the distributions.

The data are corrected for trigger and event selection cuts; event migration between (x, Q^2) intervals; QED radiative effects; track reconstruction efficiency; track selection cuts in p_T and η ; track migration between the current and target regions; and for the decay products of K_S^0 and Λ decays which are assigned to the primary vertex.

Correction factors were obtained from the Monte Carlo simulation by comparing the “true” generated distributions before the detector and trigger simulations with the “observed” distributions after these simulations followed by the same reconstruction, selection and analysis as the real data. The “true” distributions did not include the charged particle decay products of K_S^0 and Λ and charged particles produced from weakly decaying particles with a lifetime $> 10^{-8}$ s. Monte Carlo studies showed that up to 2% of the current region tracks from the reconstructed primary vertex are due to charged particles from the decay of K_S^0 and Λ . In a

separate analysis, the shape of the K_S^0 and Λ distributions are shown to be well reproduced by the Monte Carlo [45].

For the $\ln(1/x_p)$ distributions, correction factors were calculated for each $\ln(1/x_p)$ bin

$$F(\ln(1/x_p)) = \frac{1}{N_{\text{gen}}} \left(\frac{dn}{d\ln(1/x_p)} \right)_{\text{gen}} \Big/ \frac{1}{N_{\text{obs}}} \left(\frac{dn}{d\ln(1/x_p)} \right)_{\text{obs}}$$

where N_{gen} (N_{obs}) is the number of generated (observed) Monte Carlo events in the (x, Q^2) interval. The overall correction factors are greater than unity and typically < 1.3 and are independent of $\ln(1/x_p)$ around the peak position.

The correction procedure for the multiplicity distributions was performed in two stages. The dependence of this procedure on the Monte Carlo input is discussed in section 7. The first stage was to correct for track reconstruction efficiency and track migrations between the current and target regions in each $(x_{\text{rec}}, Q_{\text{rec}}^2)$ interval where x_{rec} and Q_{rec}^2 are the reconstructed values of x and Q^2 . In each interval a comparison was made between the observed multiplicity distribution $P_{n_{\text{o}}}(x_{\text{rec}}, Q_{\text{rec}}^2)$, and the generated distribution $P_{n_{\text{p}}}(x_{\text{rec}}, Q_{\text{rec}}^2)$. This comparison yielded the correction matrix $M_{n_{\text{p}}, n_{\text{o}}}(x_{\text{rec}}, Q_{\text{rec}}^2)$ with elements defined by

$$M_{n_{\text{p}}, n_{\text{o}}}(x_{\text{rec}}, Q_{\text{rec}}^2) = \frac{\text{No. of events with } n_{\text{p}} \text{ tracks generated when } n_{\text{o}} \text{ tracks were observed}}{\text{No. of events with } n_{\text{o}} \text{ tracks observed}}.$$

This matrix relates the observed to the generated distributions in each $(x_{\text{rec}}, Q_{\text{rec}}^2)$ interval by

$$P_{n_{\text{p}}}(x_{\text{rec}}, Q_{\text{rec}}^2) = \sum_{n_{\text{o}}} M_{n_{\text{p}}, n_{\text{o}}}(x_{\text{rec}}, Q_{\text{rec}}^2) \cdot P_{n_{\text{o}}}(x_{\text{rec}}, Q_{\text{rec}}^2).$$

The second stage corrected for migrations between the analysis intervals and for the acceptance of the event selection cuts using the correction factors

$$C = \frac{\rho_{\text{true}}(x_{\text{true}}, Q_{\text{true}}^2)}{\rho_{\text{rec}}(x_{\text{rec}}, Q_{\text{rec}}^2)}$$

where the ρ 's are normalised multiplicity distributions in each interval at the reconstructed level (rec) and at the generator level where no selection cuts are applied (true).

The corrected multiplicity distribution was then calculated according to the formula

$$P_{n_{\text{p}}}(x_{\text{true}}, Q_{\text{true}}^2) = C \cdot \sum_{n_{\text{o}}} M_{n_{\text{p}}, n_{\text{o}}}(x_{\text{rec}}, Q_{\text{rec}}^2) \cdot P_{n_{\text{o}}}(x_{\text{rec}}, Q_{\text{rec}}^2)$$

The overall correction factors are in the range $1.25 - 1.5$ and are dominated by the corrections from applying the matrix $M_{n_{\text{p}}, n_{\text{o}}}(x_{\text{rec}}, Q_{\text{rec}}^2)$. In the lowest two Q^2 intervals the corrections from C are of the same size as those from the matrix. The corrected multiplicity distributions in each (x, Q^2) interval are henceforth denoted by $P(n_{\text{ch}})$.

7 Systematic errors

A number of systematic checks were performed in order to investigate the sensitivity of the corrected results to features of the analysis as described previously. These can be categorised under event selection, track and vertex reconstruction, track efficiency and selection, and data correction methods.

Systematic uncertainties arising from remaining photoproduction background were studied by tightening the y_e cut from 0.95 to 0.8 and the δ cut from 35 GeV to 40 GeV. The effects of calorimeter noise on the reconstruction of x were checked by tightening the y_{JB} cut from 0.04 to 0.05. The effect of a small mismatch in electron energy scale between the Monte Carlo and data was checked by scaling the energy of the calorimeter cells associated with the electron in the Monte Carlo. The overall systematic errors associated with the event selection were negligible.

The analysis was repeated using the second approach to pattern recognition, track and vertex fitting (see section 4) applied to both the Monte Carlo sample and the data. This was found to be a significant source of systematic error. The mean multiplicity results changed by 3 – 5% in general but the effect was up to 8%. Changes to $\ln(1/x_p)_{max}$ were typically 3% although the maximum shift observed was 9%.

The efficiency of the tracking system was varied within the Monte Carlo by removing all hits from the vertex detector and 80% of hits from a random superlayer in the CTD. This is a conservative estimate of the systematic uncertainty due to inefficiencies within the detector. The largest change to the mean multiplicity was 3 – 5%. Removing the p_T and η track selection cuts produced changes in the results which were within the statistical errors. (The intervals in (x, Q^2) were chosen in order to maximise the acceptance in the current region and therefore reduce the sensitivity to these cuts.) The changes due to varying the parameters in the vertex fit were again within statistical errors.

The Monte Carlo-based correction techniques described in section 6 are model dependent. In order to investigate the size of this effect the data were corrected with two independent Monte Carlo samples, MEPS and HERWIG. The differences in the simulation of the hadronic final state implicitly test the uncertainty due to the boost reconstruction which is derived from the *DA* method. The systematic uncertainties on $\ln(1/x_p)_{max}$ and the mean multiplicity were typically between 4 – 7%. This is the largest single contribution to the overall systematic error. In the highest (x, Q^2) interval, where the statistics from Monte Carlo and data are limited, the largest change to the mean multiplicity was 17%.

Inclusion of events with a large rapidity gap in the correction procedure was investigated by correcting the data with a sum of 90% ARIADNE and 10% POMPYT events which reasonably describes the DIS data [25]. Such events are a small contribution to the inclusive distribution and as a result the $\ln(1/x_p)_{max}$ values are reduced by 1% whereas the mean multiplicities are more sensitive and increase by 3 – 5% due to the effects discussed in section 8.1.

The systematic deviations from the above checks were combined in quadrature to yield the quoted systematic errors.

8 Results

8.1 Multiplicity

The variables and distributions presented in the following sections have been corrected for detector and acceptance effects. The multiplicity distributions are binned in x and Q^2 as indicated in table 1, in the intervals $6 \times 10^{-4} < x < 5 \times 10^{-2}$ and $10 < Q^2 < 1280 \text{ GeV}^2$, where the mean values of Q range from $\simeq 4$ to 30 GeV . Figure 1 shows the measured multiplicity distributions in the current region of the Breit frame. With increasing Q the mean of the multiplicity increases. At low Q , there is a significant probability for no tracks to be found in the current region which we address later. The multiplicity distributions are compared to the ARIADNE Monte Carlo which reproduces the data in each (x, Q^2) interval.

In order to compare the multiplicity distributions at various values of Q , the scaled multiplicity distributions, $\Psi(z) = \langle n_{ch} \rangle \cdot P(n_{ch})$, are plotted as a function of $z = \frac{n_{ch}}{\langle n_{ch} \rangle}$ in figure 2 [46]. For $Q \lesssim 7 \text{ GeV}$, the distributions do not scale with Q . For $Q \gtrsim 7 \text{ GeV}$, the scaling violations are less pronounced, the distributions becoming narrower with increasing Q indicating scaling violations of the KNO variable [47] similar to those observed in e^+e^- annihilation [48].

The mean multiplicities, $\langle n_{ch} \rangle$, are shown in table 1 as a function of (x, Q^2) . Over the measured range of Q , the mean multiplicity increases by a factor of five. Comparison of the mean multiplicity in intervals of fixed Q and differing x provides a check on a possible x dependence in the current region of the Breit frame. The mean multiplicities in these intervals are the same within systematic errors.

x range	Q^2 range (GeV^2)	Q mean (GeV)	$\langle n_{ch} \rangle \pm \text{stat} \pm \text{sys}$
$0.6 - 1.2 \times 10^{-3}$	10-20	3.8	$1.12 \pm 0.02 \pm 0.15$
$1.2 - 2.4 \times 10^{-3}$	10-20	3.8	$1.25 \pm 0.02 \pm 0.25$
	20-40	5.3	$1.73 \pm 0.04 \pm 0.23$
	40-80	7.3	$2.35 \pm 0.07 \pm 0.11$
$0.24 - 1.0 \times 10^{-2}$	20-40	5.3	$1.83 \pm 0.03 \pm 0.27$
	40-80	7.4	$2.47 \pm 0.05 \pm 0.23$
	80-160	10.4	$3.05 \pm 0.09 \pm 0.31$
	160-320	14.5	$3.77 \pm 0.22 \pm 0.40$
$1.0 - 5.0 \times 10^{-2}$	320-640	20.4	$4.49 \pm 0.30 \pm 0.54$
	640-1280	29.2	$5.57 \pm 0.65 \pm 1.21$

Table 1: *Mean charged multiplicity in the current fragmentation region.*

In figure 3a the mean charged multiplicity as a function of Q is compared to the predictions of three Monte Carlo models which incorporate coherence effects. The MEPS and ARIADNE models reproduce the growth in multiplicity as observed in the data. These Monte Carlo

generators predict a higher multiplicity for the higher x range at fixed Q values. HERWIG, which includes coherent parton showers but has no explicit matrix element, also reproduces the increase with Q . Coherence suppresses the production of large multiplicity events which becomes a more noticeable effect with increasing Q .

The effects of coherence on the evolution of the parton shower have been tested by calculating the mean multiplicity with the MEPS model (with default parameter settings), as shown in figure 3b. The MEPS incoherent parton shower with independent fragmentation exhibits a faster growth of the multiplicity than seen in the data. The discontinuities in the lines correspond to predictions for two different x values at fixed Q . The growth of the incoherent case is damped when string fragmentation is used rather than independent fragmentation but not enough to agree with the data. Additional low-momentum partons produced in the incoherent shower correspond to small kinks of the Lund string. These therefore lead to relatively small differences between the incoherent and coherent case when string fragmentation is applied [49]. Overall, however, the data are best described by Monte Carlo models that include coherence in their simulations, whilst those with an incoherent shower are less successful in reproducing the multiplicity distributions and the growth of $\langle n_{ch} \rangle$ with Q .

The definition used here for associating particles with the current fragmentation region, namely $p_z < 0$, should be considered an operational definition which is unambiguous only when the produced jet and the fragmentation products are massless. If these are massive and/or if QCD radiation is included, the current and target fragmentation regions begin to merge. Consider for example the case where the struck quark branches into a quark and a gluon producing a (qg) system with mass m . Being massive, the z -momentum of the qg system becomes more positive; a special case is $m = Q$ where the qg system is at rest in the Breit frame. If, instead of the definition used in this paper, one would take the point of view that the current fragmentation should include the particles emerging from the hadronisation of the outgoing quark *and* gluon then the current region defined by $p_z < 0$ would contain only part of the fragmentation products. The Bremsstrahlung nature of QCD radiation results in partons which are mostly soft and collinear leading to small masses m . Clearly, the effect should be small if $Q \gg m$. Two exercises were made in order to estimate the size of the effect, keeping the definition of the current region as before, namely $p_z < 0$.

In the first study, the multiplicities in the current region predicted by the QPM and the ME model (i.e. first-order QCD matrix elements without parton showers) were compared. The fragmentation was performed in both cases according to the Lund scheme. In the ME calculation, QCD branching is considered if $y_{ij} > y_{cut}$, where $y_{ij} = m_{ij}^2/W^2$. Here m_{ij} is the mass of the parton system produced in the branching and W is the total centre of mass energy available for hadron production. The calculation was performed choosing a standard value of $y_{cut} = 0.015$. Note that this choice of y_{cut} corresponds to a hard branching which is a relatively rare process. The average multiplicities predicted by ME at $Q = 3.8$ GeV were found to be $\simeq 12\%$ lower than those of QPM, the difference becoming smaller as Q increased.

In the second study, this effect was investigated with data by comparing events with and without a large rapidity gap. For large rapidity gap (LRG) events, QCD radiation is suppressed compared to events without a large rapidity gap [26]. Therefore, the depopulation of the current region due to QCD radiation should also be suppressed in LRG events. Indeed, in the lowest Q interval ($Q = 3.8$ GeV) LRG events were observed to have an $\simeq 50\%$ higher multiplicity compared with non-LRG; for $Q = 7.3$ GeV the excess was $\simeq 15\%$ and for $Q > 10$ GeV the same multiplicity was observed for both event classes, within errors.

The preceding considerations suggest that for $Q > 10$ GeV the different definitions of the current region lead to approximately the same results for current fragmentation and that the data obtained here from DIS can be directly compared with those on quark fragmentation measured in e^+e^- annihilation.

In figure 4, twice the mean multiplicity is compared with inclusive mean multiplicity measurements from e^+e^- experiments [48, 50, 51, 52] for $Q \equiv \sqrt{s} > 10$ GeV. In the region of overlap the results from ZEUS and the e^+e^- experiments are in agreement, exhibiting a similar rate of growth with Q . DIS provides a larger fraction of light quarks compared with the e^+e^- case [3]. The different flavour composition of the two physics processes could, in principle, affect the comparison of these measurements. However, Monte Carlo generator studies of heavy quark production in e^+e^- using JETSET and results from e^+e^- [53] on $\langle n_{ch} \rangle$ from a sample excluding b -quarks show that these effects give rise to differences in the results that are within the quoted ZEUS errors.

8.2 Scaled momentum spectra

In figure 5 the $\ln(1/x_p)$ distributions for charged particles are shown in the same (x, Q^2) intervals as the multiplicity distributions. These distributions are approximately Gaussian in shape with mean multiplicities given by the integral of the distribution (this estimate agrees within errors with the multiplicity results, but differs slightly due to differences in the correction methods). The $\ln(1/x_p)$ distributions are compared to the ARIADNE Monte Carlo which reasonably reproduces the data in each (x, Q^2) interval.

The peak position of the distributions, $\ln(1/x_p)_{max}$, was evaluated by fitting a Gaussian over a range $\pm 1 \ln(1/x_p)$ unit around the statistical mean. This fit was motivated by the MLLA prediction for the form of the spectrum (appendix A) which can be approximated by a Gaussian distribution around the peak position at sufficiently high energies. For consistency, the same fit was performed on TASSO data [10] at different centre of mass energies and data from the OPAL experiment [11]. The $\ln(1/x_p)$ distributions published in [10] and [11] include charged particles from K_S^0 and Λ decays: Monte Carlo studies using JETSET indicated that the effect of their inclusion on the peak position was less than 0.5%. Results of the fits are shown in tables 2 and 3. Our fit to the e^+e^- data agrees, within statistical errors, with a similar fit performed by the OPAL collaboration [54]¹.

The ZEUS systematic error includes the contributions from refitting the data with the systematic variations listed in section 7. These were combined in quadrature with an estimate of the uncertainty on the fit obtained by varying the fit range and mean value by up to two bins [55]. The relative contribution to the systematic error from the fit variation is $\simeq 40\%$.

Figure 6 shows the distribution of $\ln(1/x_p)_{max}$ as a function of Q for the ZEUS data and of \sqrt{s} for the e^+e^- data. Over the range shown the peak moves from $\simeq 1.5$ to 2.8, equivalent to the position of the maximum of the corresponding momentum spectrum increasing from $\simeq 400$ to 900 MeV. The ZEUS data complement the e^+e^- results. The ZEUS data points are consistent

¹The OPAL analysis, using a modified Gaussian fit over a limited range around the peak, was not repeated due to the limited number of ZEUS data points. A modified Gaussian fit over an extended range leads to consistent results for $\ln(1/x_p)_{max}$ for the ZEUS data [55].

x range	Q^2 range (GeV 2)	Q mean (GeV)	$\ln(1/x_p)_{max} \pm$ stat \pm sys	χ^2/dof
$0.6 - 1.2 \times 10^{-3}$	10-20	3.8	$1.49 \pm 0.02 \pm 0.06$	8.2/6
$1.2 - 2.4 \times 10^{-3}$	10-20	3.8	$1.50 \pm 0.03 \pm 0.06$	4.7/6
	20-40	5.3	$1.70 \pm 0.03 \pm 0.06$	14.4/8
	40-80	7.3	$1.94 \pm 0.06 \pm 0.11$	4.4/6
$2.4 - 10.0 \times 10^{-3}$	20-40	5.3	$1.70 \pm 0.03 \pm 0.09$	12.5/6
	40-80	7.4	$1.92 \pm 0.03 \pm 0.07$	5.8/6
	80-160	10.4	$2.18 \pm 0.06 \pm 0.10$	3.2/6
	160-320	14.5	$2.25 \pm 0.10 \pm 0.23$	4.0/6
$1.0 - 5.0 \times 10^{-2}$	320-640	20.4	$2.78 \pm 0.22 \pm 0.26$	3.8/6
	640-1280	29.2	$2.85 \pm 0.21 \pm 0.24$	5.6/8

Table 2: *Fitted values of $\ln(1/x_p)_{max}$ from the ZEUS data.*

Experiment	\sqrt{s} (GeV)	$\ln(1/x_p)_{max} \pm$ stat	χ^2/dof
TASSO	14	2.356 ± 0.022	3.9/7
	22	2.667 ± 0.024	4.1/7
	35	3.020 ± 0.018	15.3/7
	44	3.104 ± 0.021	4.6/7
OPAL	91	3.594 ± 0.013	19.1/17

Table 3: *Fitted values of $\ln(1/x_p)_{max}$ from the TASSO and OPAL data.*

with those from TASSO and a clear agreement in the rate of growth of the ZEUS points with the e^+e^- data at higher Q is observed.

The increase of $\ln(1/x_p)_{max}$ can be approximated phenomenologically by the straight line fit

$$\ln(1/x_p)_{max} = b \ln(Q) + c$$

also shown in figure 6. The values obtained from the fit to the ZEUS data are $b = 0.650 \pm 0.035(\text{stat}) \pm 0.069(\text{sys})$ and $c = 0.626 \pm 0.059 \pm 0.129$. The systematic errors are calculated by re-fitting the $\ln(1/x_p)$ distributions obtained according to the variations listed in section 7 and combining the deviations from the central value of the fit parameter, b or c , in quadrature. The dominant error is from the correction of the data using the HERWIG Monte Carlo model. Removing the lowest two Q points from the fit, where the range over which the Gaussian is fitted extends well beyond the momentum range in which the MLLA is valid (see section 9), leads to no statistically significant deviation from the quoted values of b and c . The gradient extracted from the OPAL and TASSO data is $b = 0.653 \pm 0.012$ (with $c = 0.653 \pm 0.047$) which is consistent with the ZEUS result. This value is consistent with that published by OPAL, $b = 0.637 \pm 0.016$, where the peak position was extracted using an alternative method [11]. A consistent value of the gradient is therefore determined in DIS and e^+e^- annihilation experiments.

Also shown is the statistical fit to the data when $b = 1$ ($c = 0.054 \pm 0.012$) which would be the case if the QCD cascade was of an incoherent nature, dominated by cylindrical phase space. (A discussion of phase space effects is given in [49].) In such a case, the logarithmic particle momentum spectrum would be peaked at a constant value of momentum, independent of Q . The observed gradient is clearly inconsistent with $b = 1$ and therefore inconsistent with cylindrical phase space.

In figure 7a the measurements are compared with the results from the ARIADNE, HERWIG and MEPS Monte Carlo simulations. These models describe the $\ln(1/x_p)$ distributions and the evolution of their maximum as well as the multiplicity distributions shown in section 8.1. As in the case of $\langle n_{ch} \rangle$, the difference between the coherent and incoherent growth of $\ln(1/x_p)_{max}$ is found to be reduced when string fragmentation is used rather than independent fragmentation (figure 7b). Again, the $\ln(1/x_p)$ distributions and the growth of $\ln(1/x_p)_{max}$ with Q are well-described by Monte Carlo models that include coherence in their simulations, whilst those with an incoherent shower are less successful in describing the data.

In contrast to the $\langle n_{ch} \rangle$ measurements, the $\ln(1/x_p)_{max}$ values change only slightly when only the rapidity gap events are used, with a maximum negative shift of $\simeq 5\%$ in the lowest (x, Q^2) interval. Effects due to primary heavy-quark production were also found to be negligible.

The evolution of $\ln(1/x_p)_{max}$ seen in DIS agrees with the e^+e^- data. The growth is at a slower rate than that expected from cylindrical phase space, indicative of coherence. Monte Carlo models including coherence effects describe the $\ln(1/x_p)_{max}$ values and the $\ln(1/x_p)$ distributions better than those with an incoherent behaviour. The rate of growth with increasing Q of $\langle n_{ch} \rangle$ and $\ln(1/x_p)_{max}$ in the current region of the Breit frame agrees with e^+e^- data in the region of overlap (i.e. above 10 GeV) indicating that the fragmentation of quarks in DIS is similar to that of quarks produced in e^+e^- annihilation.

9 Comparisons with MLLA

In order to test the predictions of the MLLA (Modified Leading Log Approximation) and LPHD (Local Parton Hadron Duality) at different energies, fits to the individual $\ln(1/x_p)$ distributions were performed in the chosen (x, Q^2) intervals. The evolution of these distributions with Q is also predicted within the framework of the MLLA.

In the high energy limit, MLLA calculations predict the momentum distribution of soft gluons, \bar{D}^{lim} , radiated by a quark of energy $E = Q/2$ according to equation (4) given in appendix A. \bar{D}^{lim} is known as the limiting spectrum. Invoking LPHD, the $\ln(1/x_p)$ distribution of the hadrons is given by

$$\frac{1}{\sigma} \frac{d\sigma}{d(\ln(1/x_P))} = \kappa^{\text{ch}} \bar{D}^{\text{lim}}(\ln(1/x_P), Y) \quad (1)$$

where $Y = \ln(Q/2\Lambda)$. The Λ in the expression is an effective scale parameter and not the standard QCD scale, e.g. $\Lambda_{\overline{\text{MS}}}$. This MLLA prediction is valid in the range $0 \lesssim \ln(1/x_p) \lesssim Y$, a region where pQCD can be applied. The normalisation factor κ^{ch} is energy independent within the framework of LPHD. In addition, the charged multiplicity can be expressed as

$$\langle n_{ch} \rangle = \kappa^{\text{ch}} \mathcal{N}(Y) \quad (2)$$

where $\mathcal{N}(Y)$ is the integral of \bar{D}^{lim} given by equation (5) in appendix A and represents the soft gluon multiplicity.

The evolution of $\ln(1/x_p)_{\text{max}}$ with Q is a function of Λ and is given by

$$\ln(1/x_p)_{\text{max}} = \frac{1}{2}Y + c_2\sqrt{Y} - c_2^2 + \left(\mathcal{O}(Y^{-1/2})\right) \quad (3)$$

where c_2 is a constant calculated from the number of flavours and colours. Taking the active number of flavours to be 3, the value of the constant c_2 is 0.52. The term $\mathcal{O}(Y^{-1/2})$ describes higher-order effects.

The functional form of equation (1) was fitted to the $\ln(1/x_p)$ distributions. This equation has two free parameters, κ^{ch} and Λ . The fit was performed for each (x, Q^2) interval in the range $0 < \ln(1/x_p) < \ln(Q/2p_0)$ where $p_0 = 400$ MeV. This restriction limits the comparisons of MLLA at the lower Q values. Due to the restricted range of the fit very little of the peak region of the lowest Q value is included: these intervals are therefore excluded from the following fits. The results of these fits are shown in table 4.

x range	Q^2 range (GeV 2)	Q mean (GeV)	$\Lambda \pm \text{stat}$ (MeV)	$\kappa^{\text{ch}} \pm \text{stat}$
$1.2 - 2.4 \times 10^{-3}$	20-40	5.3	330 ± 29	1.25 ± 0.05
	40-80	7.3	323 ± 20	1.28 ± 0.07
$2.4 - 10.0 \times 10^{-3}$	20-40	5.3	313 ± 28	1.21 ± 0.04
	40-80	7.4	296 ± 19	1.30 ± 0.05
	80-160	10.4	296 ± 28	1.25 ± 0.06
	160-320	14.5	311 ± 48	1.31 ± 0.10
$1.0 - 5.0 \times 10^{-2}$	320-640	20.4	210 ± 54	1.14 ± 0.10
	640-1280	29.2	266 ± 81	1.18 ± 0.16

Table 4: *Fitted values of Λ and κ^{ch} .*

Approximately the same value of Λ is found at all values of Q . The values of Λ are combined to give a weighted mean value of

$$\Lambda = 306 \pm 10 \text{ (stat)} \pm 30 \text{ (sys)} \text{ MeV.}$$

The fits in each interval are also consistent with a single value of κ^{ch} with a mean value of κ^{ch} given by

$$\kappa^{\text{ch}} = 1.25 \pm 0.02 \text{ (stat)} \pm 0.09 \text{ (sys).}$$

The experimental systematic errors are calculated by re-fitting the $\ln(1/x_p)$ distributions obtained according to the variations listed in section 7 and combining the deviations from the central values of the fit parameters, Λ and κ^{ch} , in quadrature. The dominant error is from the correction of the data using the HERWIG Monte Carlo model. The absolute value of the correlation coefficient between Λ and κ^{ch} from the fits was typically ~ 0.35 . Equation (1) was

re-fitted with p_0 varying from 200 to 500 MeV, yielding consistent results within the quoted systematic errors. Similarly, this equation was re-fitted with Λ fixed at its mean value and κ^{ch} as a free parameter. The values of κ^{ch} remain the same within the statistical accuracy of the fit with little degradation in the χ^2 .

The results of the fits to the MLLA limiting spectrum using the mean values of Λ and κ^{ch} above are shown in figure 8. The data are reasonably well described by the limiting spectrum with single values of Λ and κ^{ch} over a large range in Q . The overall χ^2/dof for all the ZEUS data is 152/106. At higher values of $\ln(1/x_p)$, beyond the range of the fit, the MLLA spectrum underestimates the multiplicity.

The values measured by OPAL, fitting their data over a limited momentum range, were $\Lambda = 253 \pm 30$ MeV and $\kappa^{\text{ch}} = 1.44 \pm 0.01$. In order to compare with the ZEUS measurement, their value of κ^{ch} has been divided by a colour factor of 4/9 and by a factor of 2 to account for the quark and anti-quark pair, factors which OPAL absorbed into their value quoted in [11]. The inclusion of decay-particles from K_S^0 and Λ in the OPAL data contributes 10% to the multiplicity [51] and can account for the higher value of κ^{ch} . The value of Λ is also sensitive to this but to a lesser degree. Monte Carlo studies using JETSET indicated that the effect of their inclusion on the value of Λ was less than 10 MeV.

In order to check the consistency of κ^{ch} , equation (2) was fitted to $\langle n_{ch} \rangle$ as a function of Q . Taking the value of Λ extracted from the individual $\ln(1/x_p)$ distributions, $\Lambda = 306$ MeV, the fitted value of $\kappa^{\text{ch}} = 1.78 \pm 0.02$ (stat) was determined. This value of κ^{ch} is significantly higher than that extracted from the $\ln(1/x_p)$ distributions. Equation (2) is derived from the integration of equation (1), this expression underestimates the data at large $\ln(1/x_p)$ (see figure 8). At the relatively low Q values of the ZEUS data, $Q \lesssim 7$ GeV, this accounts for a significant fraction of the total multiplicity where the MLLA prediction, taken outside its range of validity, underestimates the data. The underestimate of the predicted parton multiplicity by the MLLA is therefore compensated by an increase in the value of κ^{ch} .

In order to check the consistency of Λ , the evolution of $\ln(1/x_p)_{\text{max}}$ was investigated. The value of Λ hardly influences the slope of $\ln(1/x_p)_{\text{max}}$ in equation (3), but gives the absolute value of $\ln(1/x_p)_{\text{max}}$ at a given Q value. This is highly correlated with the higher-order term $\mathcal{O}(Y^{-1/2})$ in equation (3) and therefore this term is neglected in the following fits. The Gaussian fits which determine the $\ln(1/x_p)_{\text{max}}$ values described in section 8.2 extend to momentum values lower than the measured Λ . In order to compare with MLLA calculations, the peak position of the $\ln(1/x_p)$ distribution was extracted again, using a Gaussian symmetric around the estimated peak position. The range of the fit was from $(2L_0 - Y)$ to Y where L_0 is the estimated peak position, calculated from equation (3) neglecting the $\mathcal{O}(Y^{-1/2})$ term and assuming $Y = \ln(Q/2p_0)$, where $p_0 = 306$ MeV. A value of $\Lambda = 284 \pm 8$ (stat) MeV is found, consistent with the value extracted from the fit of the individual plots. This compares to a value of $\Lambda = 212 \pm 20$ MeV from the evolution of the TASSO and OPAL data as extracted by OPAL. (OPAL fit equation (3) with c_2 as a free parameter; a high correlation was found between c_2 and Λ when fitting the ZEUS data.)

Although the growth of the multiplicity cannot be consistently described by the MLLA and LPHD, a single value of Λ and κ^{ch} can describe the $\ln(1/x_p)$ distributions over a range of Q values from ~ 5 to 30 GeV. The values obtained are consistent with those extracted at $\sqrt{s} = 91$ GeV by the OPAL experiment. The evolution of $\ln(1/x_p)_{\text{max}}$ with Q also gives a consistent value of Λ , again compatible with the OPAL and TASSO results.

10 Conclusions

Charged particle distributions have been measured in the current region of the Breit frame in DIS over a wide range of Q values. In the framework of the Monte Carlo models, the best description of the data is achieved by those incorporating coherence effects where the production of soft particles and the growth of the mean multiplicity is suppressed relative to the incoherent case. Modified Leading Log Approximation (MLLA) calculations have been shown to describe the $\ln(1/x_p)$ distributions in the range $5 \lesssim Q \lesssim 30$ GeV using single values of κ^{ch} , which relates the observed hadron distributions to the calculated parton distributions, and of Λ , an effective scale parameter of the QCD calculations.

A comparison of these charged particle distributions with those from e^+e^- annihilation experiments has been performed. For $Q > 10$ GeV a growth in $\langle n_{ch} \rangle$ is observed with Q which is similar to the growth in e^+e^- experiments as a function of \sqrt{s} . The evolution of $\ln(1/x_p)_{\text{max}}$ has been measured and is consistent with that observed in e^+e^- experiments. The fragmentation properties of the struck quark from the proton in DIS that have been studied here are similar to those from quarks created in e^+e^- annihilation. The observed charged particle spectra are therefore consistent with the universality of quark fragmentation.

Acknowledgements

The experiment was made possible by the inventiveness and the diligent efforts of the HERA machine group who continued to run HERA most efficiently during 1993.

The design, construction and installation of the ZEUS detector has been made possible by the ingenuity and dedicated effort of many people from inside DESY and from the home institutes who are not listed as authors. Their contributions are acknowledged with great appreciation.

The strong support and encouragement of the DESY Directorate has been invaluable.

We also gratefully acknowledge the support of the DESY computing and network services.

We would like to thank V. Khoze and B. Webber for valuable discussions.

Appendix A

MLLA formulæ

QCD predicts the form of the soft gluon momentum distribution at a fixed energy and describes the energy evolution of the spectrum, including the multiplicity and the peak maximum.

In the high energy limit, MLLA (pQCD) calculations predict [8] the momentum distribution of soft gluons from a quark with energy E according to the following formula, in which x_P is the momentum scaled with E ,

$$\bar{D}^{\text{lim}}(\ln(1/x_P), Y) = \frac{4C_f}{b} \Gamma(B) \int_{-\pi/2}^{\pi/2} \frac{d\tau}{\pi} e^{-B\alpha} \left[\frac{\cosh \alpha + (1 - 2\zeta) \sinh \alpha}{\frac{4N_c}{b} Y \frac{\alpha}{\sinh \alpha}} \right]^{B/2} \cdot I_B \left(\sqrt{\frac{16N_c}{b} Y \frac{\alpha}{\sinh \alpha} [\cosh \alpha + (1 - 2\zeta) \sinh \alpha]} \right) \quad (4)$$

where C_f , b and B are constants based on the number of flavours and colours. For the number of flavours, $N_f = 3$, and the number of colours, $N_c = 3$, the constants C_f , b and B are equal to $4/3$, 9 , and 1.247 respectively. $Y = \ln(E/\Lambda)$, where Λ is an effective scale parameter. For the case of DIS, in the current fragmentation region, $E = Q/2$ and for e^+e^- , $E = \sqrt{s}/2$. Γ denotes the Gamma function and I_B is a modified Bessel function of order B . The variable α is given by $\alpha = \alpha_0 + i\tau$, where α_0 is determined by

$$\tanh \alpha_0 = 2\zeta - 1$$

and $\zeta = 1 - \ln(1/x_P)/Y$. The integral, which is a representation of the confluent hypergeometric function, is performed over τ . \bar{D}^{lim} is known as the limiting spectrum which is expressed in a form that is suitable for numerical integration.

From the limiting spectrum the soft gluon multiplicity can be calculated as

$$\mathcal{N}(Y) = \frac{C_f}{N_c} \Gamma(B) \left(\frac{z}{2} \right)^{-B+1} I_{B+1}(z) \quad (5)$$

where $z = \sqrt{\frac{16N_c}{b} Y}$.

References

- [1] R.P. Feynman, "Photon-Hadron Interactions", Benjamin, N.Y. (1972).
- [2] Yu. Dokshitzer et al., Rev. Mod. Phys. 60 (1988) 373.
- [3] A. V. Anisovich et al., Il Nuovo Cimento, A106 (1993) 547.
- [4] K. Charchula, J. Phys. G19 (1993) 1587.
- [5] A. Bassutto et al., Nucl. Phys. B207 (1982) 189.
- [6] A. Mueller, Nucl. Phys. B213 (1983) 85.
- [7] B. Webber, Nucl. Phys. B238 (1984) 492.
- [8] Yu. Dokshitzer, V. Khoze, A. Mueller and S. Troyan, "Basics of Perturbative QCD", Editions Frontières, Gif-sur-Yvette, France (1991).
- [9] Ya. Azimov et al., Z. Phys. C27 (1985) 65.
- [10] TASSO Collab., W. Braunschweig et al., Z. Phys. C47 (1990) 187;
TASSO Collab., W. Braunschweig et al., Z. Phys. C22 (1984) 307.
- [11] OPAL Collab., M. Akrway et al., Phys. Lett. B247 (1990) 617.
- [12] L3 Collab., B. Adeva et al., Phys. Lett. B259 (1991) 179.
- [13] M. Derrick et al., Phys. Lett. B91 (1980) 470.
- [14] The ZEUS Detector, Status Report 1993, DESY 1993.
- [15] ZEUS Collab., M. Derrick et al., Phys. Lett. B293 (1992) 465.
- [16] C. Alvisi et al., Nucl. Instrum. Methods A305 (1991) 30.
- [17] C.B. Brooks et al., Nucl. Instrum. Methods A283 (1989) 477;
N. Harnew et al., ibid. A279 (1989) 290;
B. Foster et al., ibid. A338 (1994) 254.
- [18] A. Andreesen et al., Nucl. Instrum. Methods A309 (1991) 101;
A. Bernstein et al., ibid. A336 (1993) 23;
A. Caldwell et al., ibid. A321 (1992) 356.
- [19] J. Andruszkow et al., DESY 92-066.
- [20] W.H. Smith et al., DESY 94-183, submitted to Nucl. Instrum. Methods.
- [21] ZEUS Collab., M. Derrick et al., DESY 94-143, submitted to Z. Phys. C.
- [22] ZEUS Collab., M. Derrick et al., Z. Phys. C59 (1993) 231.
- [23] ZEUS Collab., M. Derrick et al., Phys. Lett. B315 (1993) 481.
- [24] ZEUS Collab., M. Derrick et al., Phys. Lett. B316 (1993) 412.

- [25] ZEUS Collab., M. Derrick et al., *Phys. Lett.* B332 (1994) 228.
- [26] ZEUS Collab., M. Derrick et al., *Phys. Lett.* B338 (1994) 483.
- [27] F. Jacquet and A. Blondel, Proceedings of the study for an ep facility in Europe, DESY 79/48 (1979) 391.
- [28] S. Bentvelsen, J. Engelen, P. Kooijman, Proceedings of the 1991 Workshop on Physics at HERA, DESY Vol. 1 (1992) 23.
- [29] R.E. Kalman, *J. Basic Eng.* 82 (1960) 35;
 R.E. Kalman and R.S. Bucy, *ibid.* 83 (1961) 95;
 P. Billoir and S. Qian, *Nucl. Instrum. Methods* A294 (1990) 219;
 P. Billoir and S. Qian, *ibid.* A295 (1990) 492.
- [30] P. Billoir and S. Qian, *Nucl. Instrum. Methods* A311 (1992) 139.
- [31] R. Brun et al., GEANT3, CERN DD/EE/84-1 (1987).
- [32] A. Kwiatkowski, H. Spiesberger and H.-J. Möhring, Proceedings of the 1991 Workshop on Physics at HERA, DESY Vol. 3 (1992) 1294.
- [33] G. Ingelman, Proceedings of the 1991 Workshop on Physics at HERA, DESY Vol. 3 (1992) 1366.
- [34] K. Charchula, G. Schuler and H. Spiesberger, CERN-TH.7133/94.
- [35] L. Lönnblad, *Comp. Phys. Comm.* 71 (1992) 15.
- [36] B. Andersson et al., *Phys. Rep.* 97 (1983) 31.
- [37] T. Sjöstrand, *Comp. Phys. Comm.* 39 (1986) 347;
 T. Sjöstrand and M. Bengtsson, *ibid.* 43 (1987) 367.
- [38] G. Marchesini et al., *Comp. Phys. Comm.* 67 (1992) 465.
- [39] G. Marchesini and B. Webber, *ibid.* B310 (1988) 461.
- [40] A.D. Martin, W.J. Stirling and R.G. Roberts, *Phys. Lett.* B306 (1993) 145.
- [41] M. Glück, E. Reya and A. Vogt, *Phys. Lett.* B306 (1993) 391.
- [42] H1 Collab., I. Abt et al., *Nucl. Phys.* B407 (1993) 515.
- [43] P. Bruni and G. Ingelman, DESY 93-187; Proceedings of the Europhysics Conference on HEP, Marseille 1993, 595.
- [44] N.N. Nikolaev and B.G. Zakharov, *Z. Phys.* C53 (1992) 331;
 A.Solano, PhD thesis, University of Torino (1993).
- [45] ZEUS Collab., M. Derrick et al., ICHEP94 Ref. 0670.
- [46] Z. Koba, H.B. Nielsen and P. Olesen, *Nucl. Phys.* B40 (1972) 317.
- [47] R. Szwed, G. Wrocha and A.K. Wroblewski, *Mod. Phys. Lett.* A6 (1991) 245.

- [48] TASSO Collab., W. Braunschweig et al., *Z. Phys. C*45 (1989) 193.
- [49] E.R. Boudinov, P.V. Chliapnikov and V.A. Uvarov, *Phys. Lett. B*309 (1993) 210.
- [50] PLUTO Collab., Ch. Berger et al., *Phys. Lett. B*95 (1980) 313.
- [51] OPAL Collab., P.D. Acton et al., *Z. Phys. C*53 (1992) 539.
- [52] HRS Collab., M. Derrick et al., *Phys. Rev. D*34 (1986) 3304.
- [53] OPAL Collab., R. Akers et al., *Z. Phys. C*61 (1994) 209.
- [54] H. Kreutzmann, PhD thesis, University of Bonn (1990).
- [55] V.A. Jamieson, PhD thesis, University of Glasgow (1994).

$1/N \frac{dN}{dn_{ch}}$

ZEUS 1993

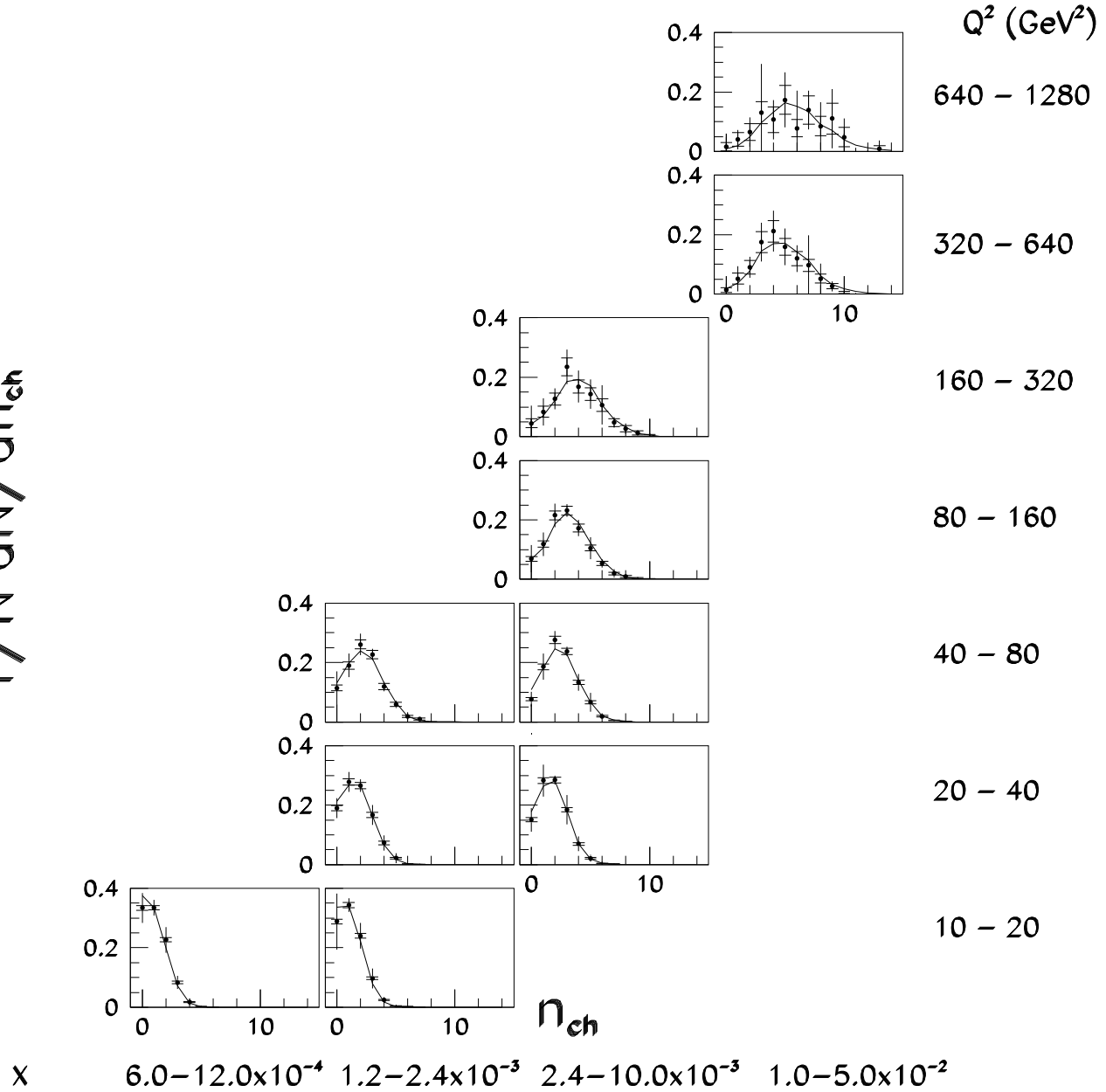


Figure 1: Charged multiplicity distributions in the current region of the Breit frame as a function of (x, Q^2) . Statistical errors are indicated by the inner error bar bounded by the horizontal bars. The outer error bars show the statistical and systematic errors added in quadrature. The ZEUS data are compared to the predictions of the ARIADNE Monte Carlo.

ZEUS 1993

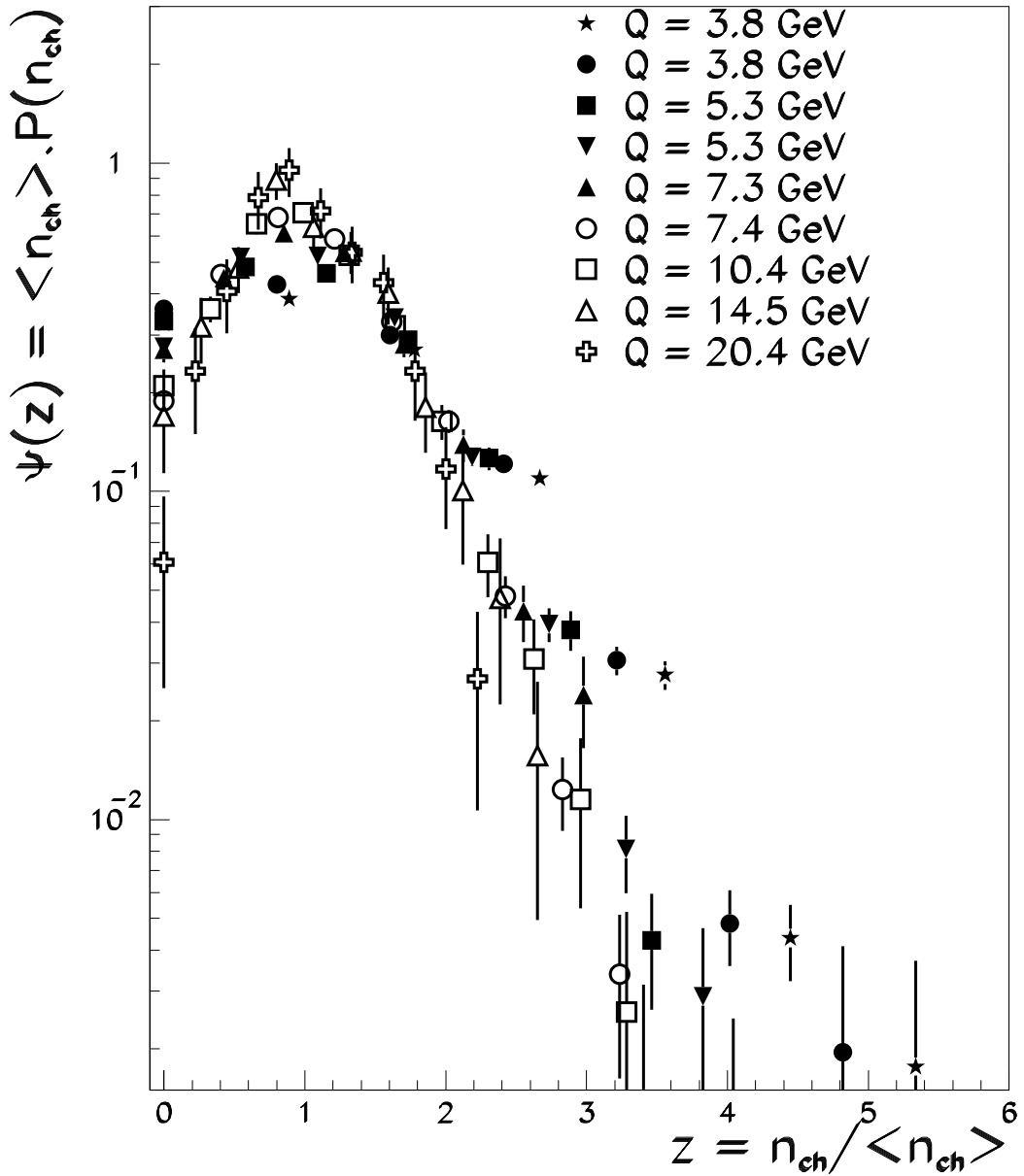


Figure 2: The KNO distribution in the current region of the Breit frame as measured by ZEUS. The values of Q correspond to the x -intervals shown in table 1. The highest (x, Q^2) interval is omitted for the sake of clarity. Statistical errors only are indicated.

ZEUS 1993

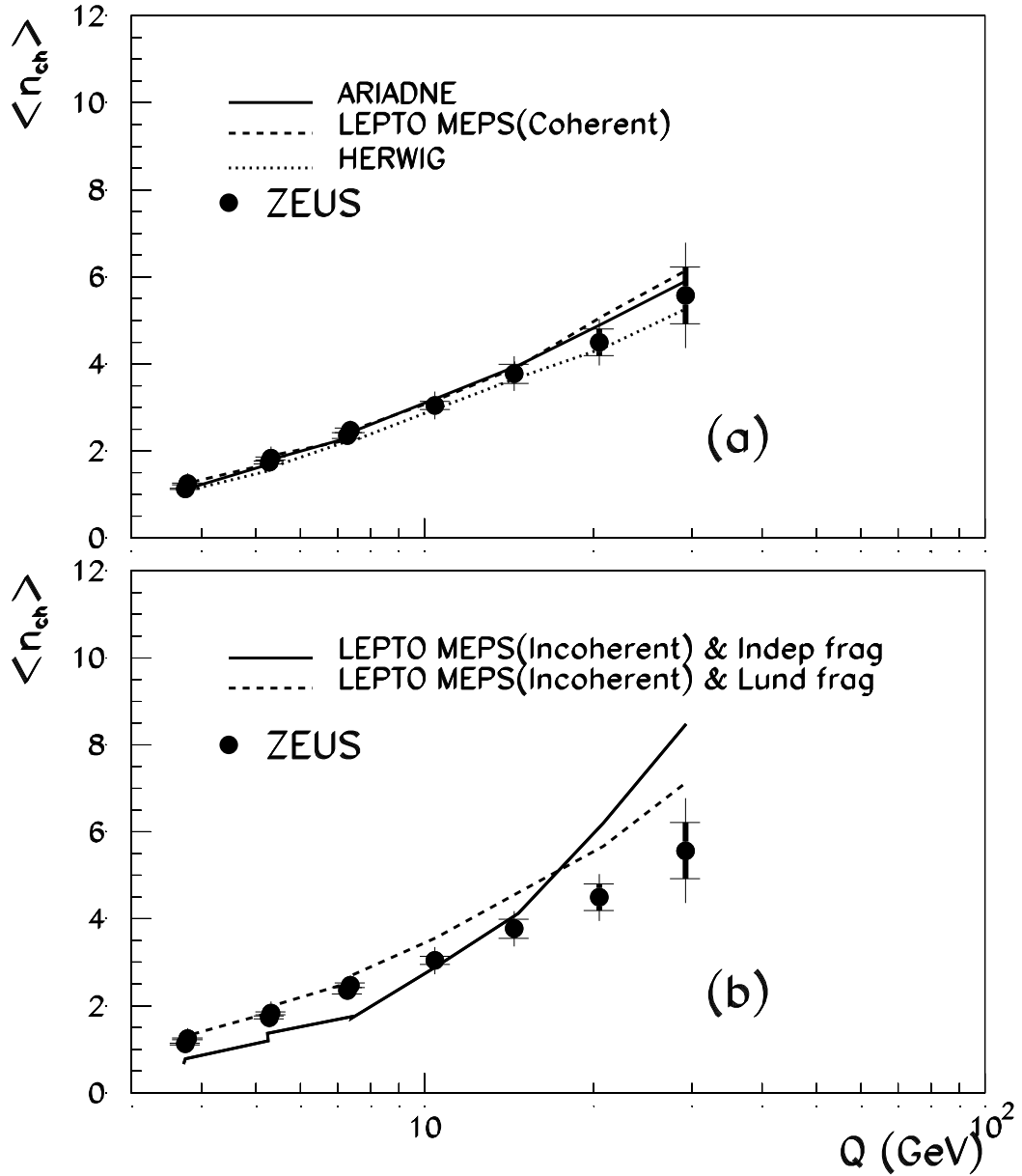


Figure 3: $\langle n_{ch} \rangle$ as a function of Q for the x -intervals shown in table 1. The ZEUS data are compared to various Monte Carlo models. The data in figures (a) and (b) are the same. The discontinuities in the Monte Carlo curves correspond to predictions for two different x values at fixed Q . The line connects the lower- x to the higher- x point with increasing Q .

ZEUS 1993

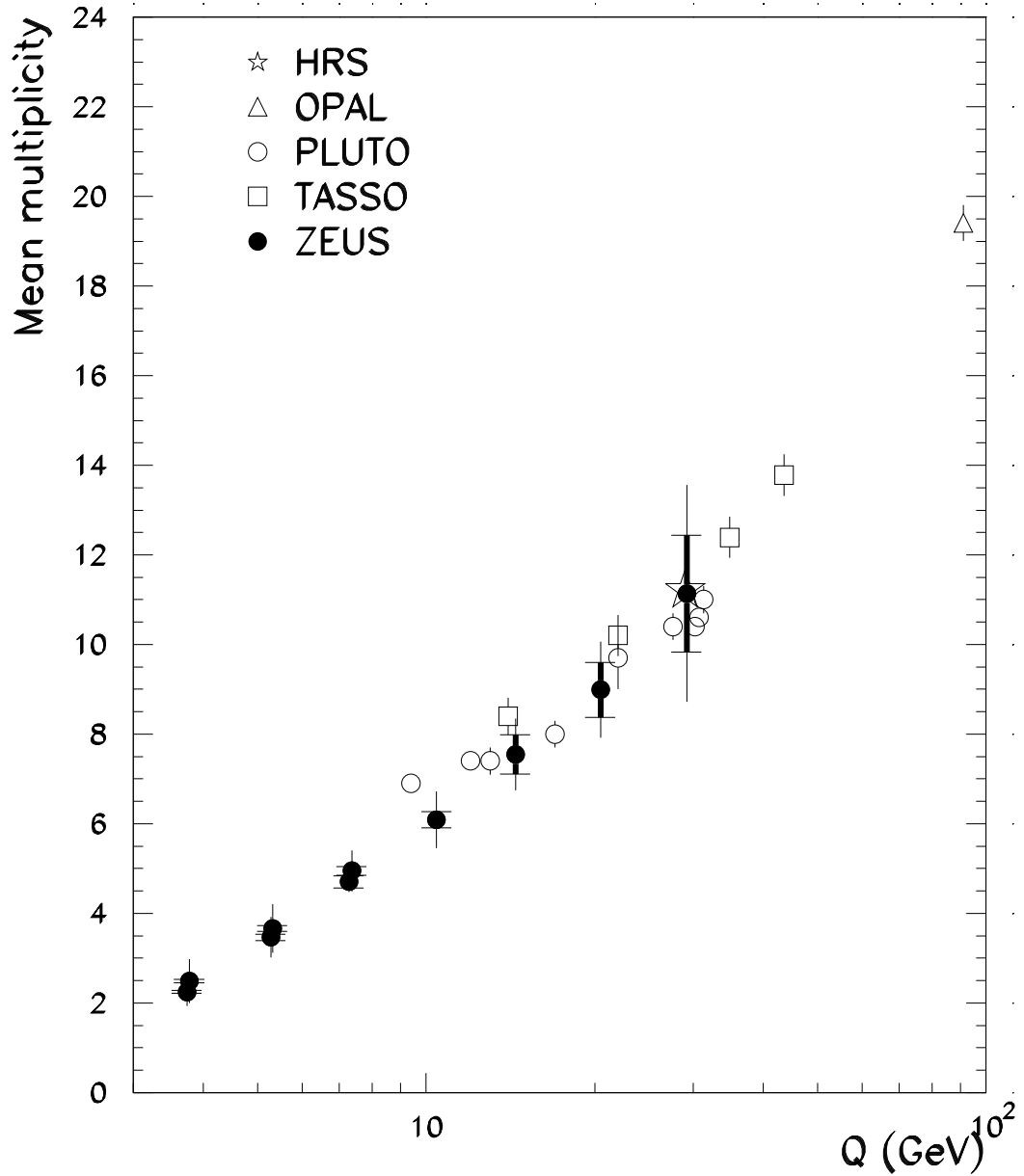


Figure 4: Mean charged multiplicity as a function of Q . Twice the measured ZEUS multiplicity, $2 \cdot \langle n_{ch} \rangle$, is compared to $\langle n_{ch} \rangle$ results from HRS, OPAL, PLUTO and TASSO. All data were corrected for K_S^0 and Λ decays.

ZEUS 1993

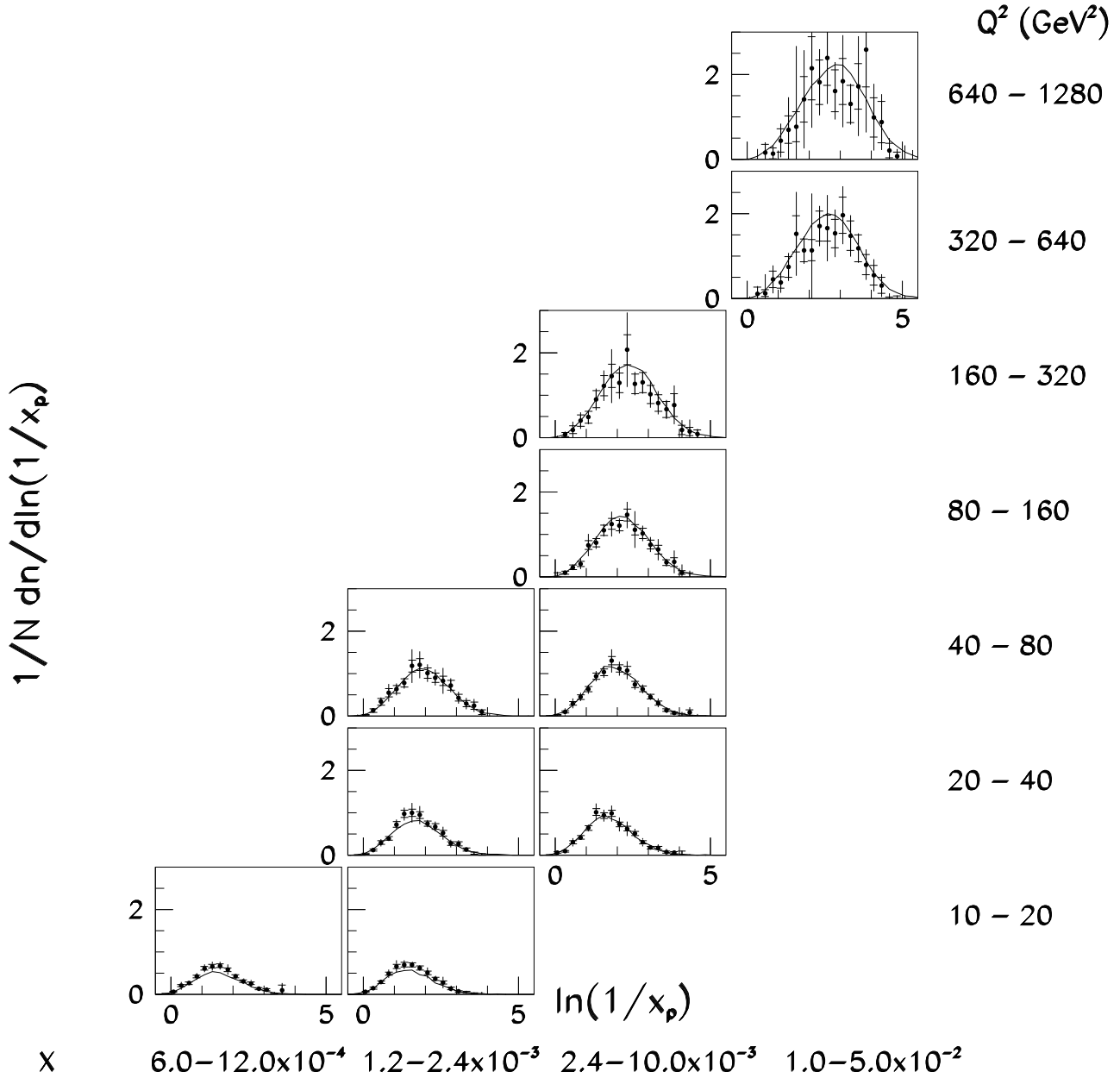


Figure 5: $\ln(1/x_p)$ distributions in the current region of the Breit frame as a function of (x, Q^2) . Statistical errors are indicated by the inner error bar bounded by the horizontal bars. The outer error bars show the statistical and systematic errors added in quadrature. The ZEUS data are compared to the predictions of the ARIADNE Monte Carlo.

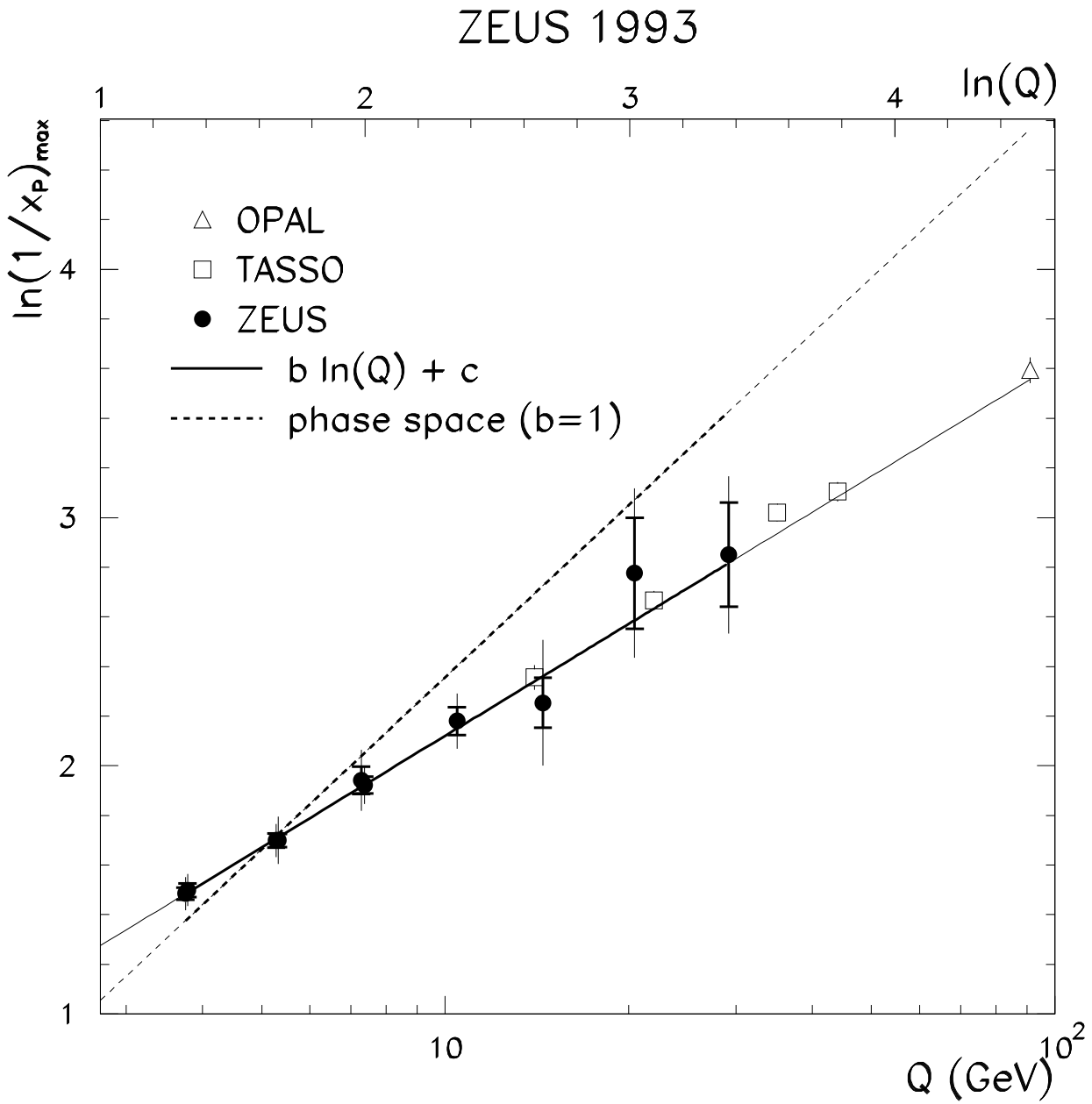


Figure 6: $\ln(1/x_p)_{\text{max}}$ as a function of Q for the x -intervals shown in table 1. The ZEUS data are compared to results from OPAL and TASSO. A straight line fit of the form $\ln(1/x_p)_{\text{max}} = b \ln(Q) + c$ to the ZEUS $\ln(1/x_p)_{\text{max}}$ values is indicated as well as the line corresponding to $b = 1$, discussed in the text.

ZEUS 1993

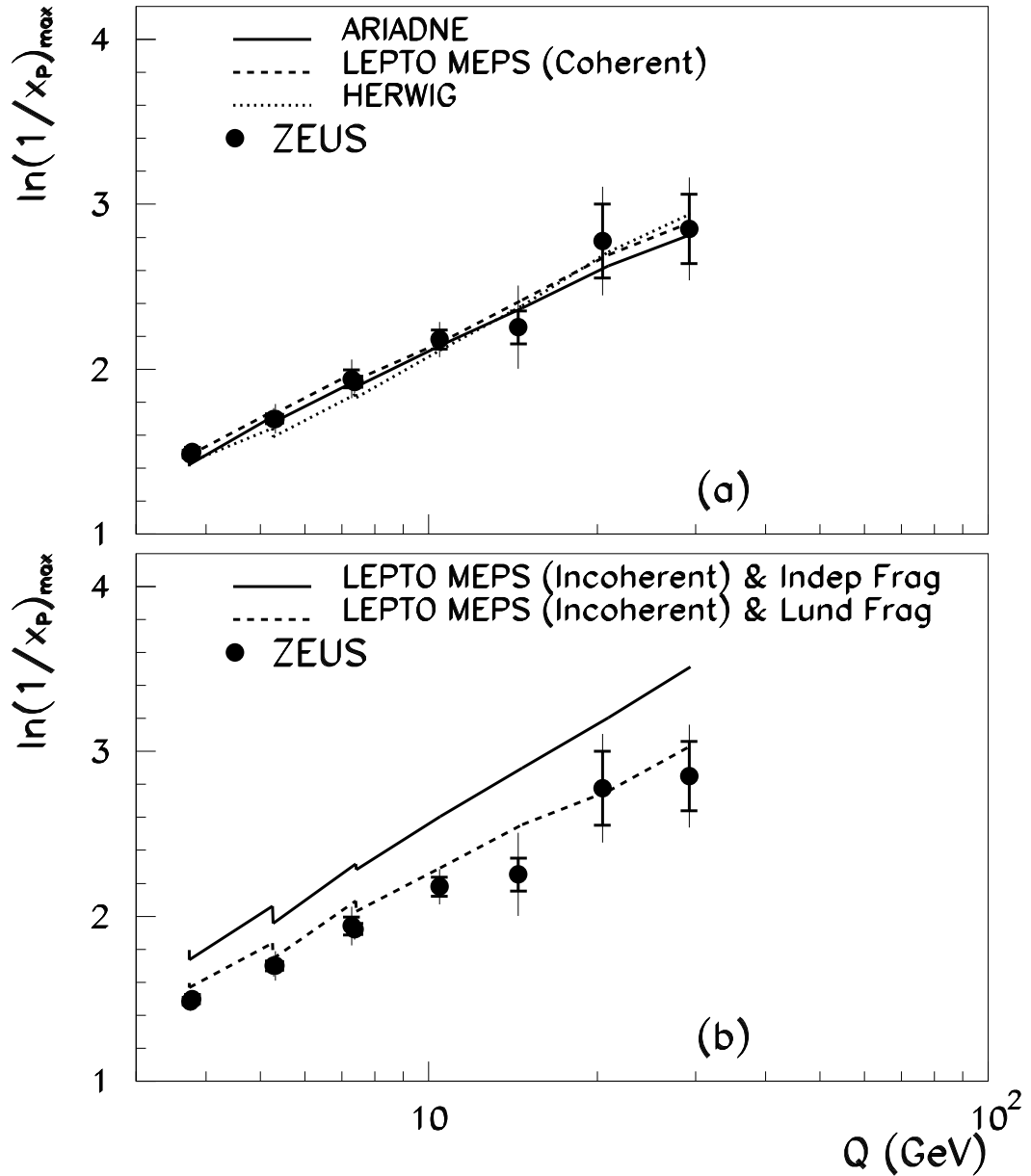


Figure 7: $\ln(1/x_p)_{\max}$ as a function of Q . The ZEUS data are compared to various Monte Carlo models. The data in figures (a) and (b) are the same. The discontinuities in the Monte Carlo curves correspond to predictions for two different x values at fixed Q .

ZEUS 1993

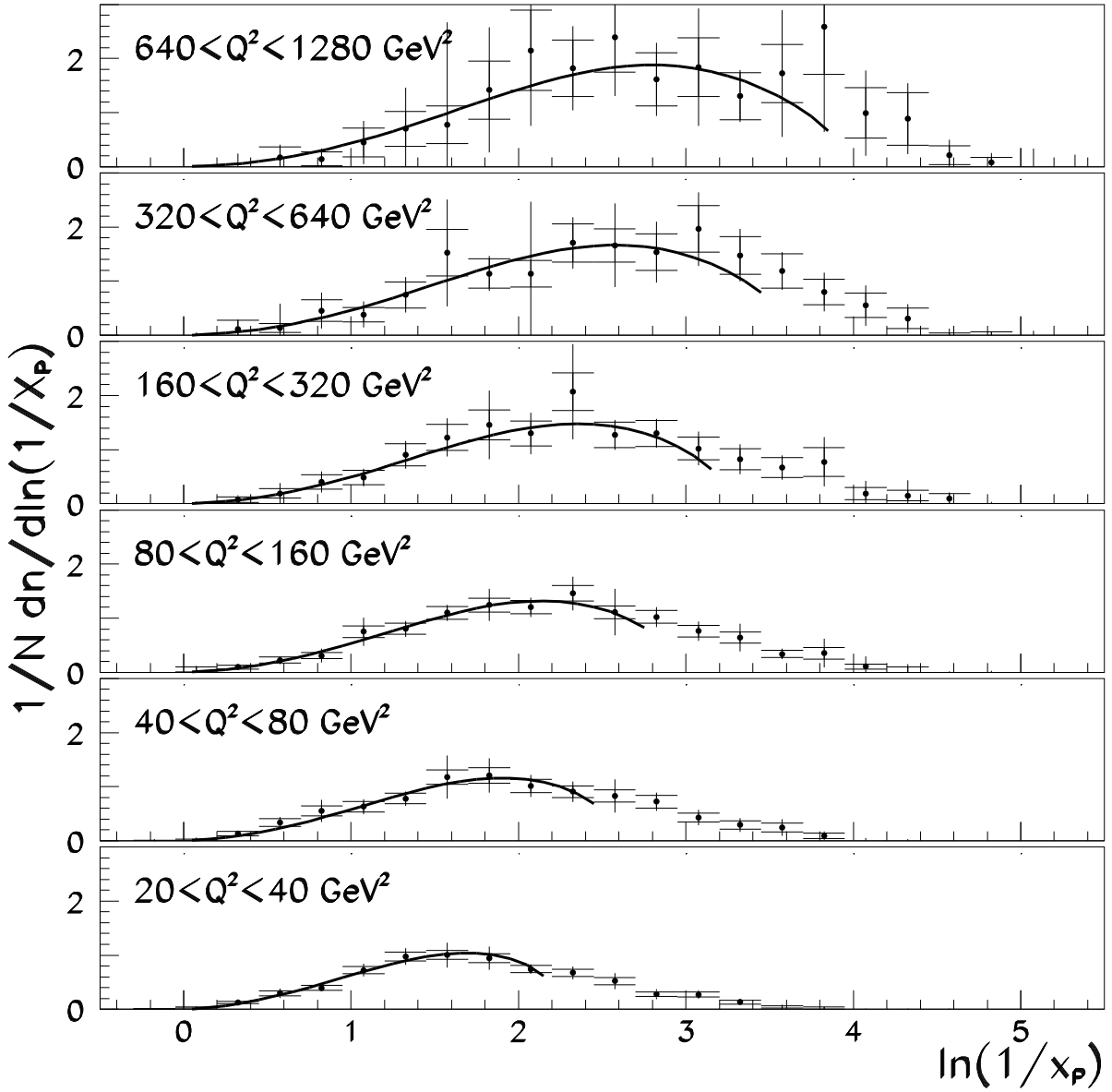


Figure 8: $\ln(1/x_p)$ distributions in the current region of the Breit frame as a function of Q^2 . The ZEUS data are compared to the MLLA limiting spectrum in the range $0 < \ln(1/x_p) < \ln(Q/2\Lambda)$ with $\Lambda = 306\text{MeV}$ and $\kappa^{\text{ch}} = 1.25$. For clarity, only the lower x range is shown in the two lowest Q^2 intervals.